Study of the role of porosity on the functional properties of $(Ba,Sr)TiO_3$ ceramics

Roxana Stanculescu, Cristina E. Ciomaga, Leontin Padurariu, Pietro Galizia, Nadejda Horchidan, Claudio Capiani, Carmen Galassi, Liliana Mitoseriu

PII: S0925-8388(15)01000-2
DOI: http://dx.doi.org/10.1016/j.jallcom.2015.03.252
Reference: JALCOM 33889

To appear in: *Journal of Alloys and Compounds*

Received Date: 19 December 2014
Revised Date: 26 February 2015
Accepted Date: 30 March 2015

Please cite this article as: R. Stanculescu, C.E. Ciomaga, L. Padurariu, P. Galizia, N. Horchidan, C. Capiani, C. Galassi, L. Mitoseriu, Study of the role of porosity on the functional properties of $(Ba,Sr)TiO_3$ ceramics, *Journal of Alloys and Compounds* (2015), doi: http://dx.doi.org/10.1016/j.jallcom.2015.03.252

Study of the role of porosity on the functional properties of $(Ba,Sr)TiO_3$ ceramics

Roxana Stanculescu[1], Cristina E. Ciomaga[1*], Leontin Padurariu[1**], Pietro Galizia[2], Nadejda Horchidan[1], Claudio Capiani[2], Carmen Galassi[2], and Liliana Mitoseriu[1***]

[1]*Dielectrics, Ferroelectrics & Multiferroics, Department of Physics, "Al. I. Cuza" University of Iasi, 11 Bv. Carol I, 700506 Iasi, Romania*

[2]*CNR -ISTEC, Via Granarolo no. 64, I-48018 Faenza, Italy*

Corresponding authors: [*]cristina.ciomaga@uaic.ro, [**]leontin.padurariu@uaic.ro , [***]lmtsr@uaic.ro

Phone: +40232201201 int 2406

Abstract

The role of porosity on the low and high field dielectric properties was studied in $Ba_{0.70}Sr_{0.30}TiO_3$ ceramics with various porosity levels obtained by using lamellar graphite as sacrificial template. The permittivity decreases with increasing porosity, from around ε~7690 (dense ceramic) down to 380 (ceramic with 29% porosity), while preserving the Curie temperature at about 35°C. The effective permittivity was discussed by using Effective Medium Approximation and Finite Element Method approaches. The role of porosity and specific microstructural characteristics induced by the pore forming addition, from closed porosity (0-3) towards a combined (0-3, 2-2) with lamellar-type of microstructures for the most porous ceramics was taken into consideration. All the

investigated ceramics preserve a high level of tunability as in the dense material, irrespective of the porosity level, while the zero field permittivity was decreased to a few hundreds.

1. Introduction

$BaTiO_3$ (BT)-based materials are among the most used oxide systems in microelectronics, in particular for tunable elements, pyroelectric, piezoelectric, electro-optic and charge storage applications [1-7]. BT and its solid solutions are lead-free ferroelectrics with a wide range of permittivity varying from a few hundreds to thousands, depending mainly on the doping level, microstructural characteristics, density and grain size, temperature range and applied field [7-11]. $Ba_{1-x}Sr_xTiO_3$ (BST) solid solution is one of the most favorable electronic materials due to its composition-dependent Curie temperature in a large temperature range and excellent electrical properties. The BST solid solutions present large level of tunability of their dielectric permittivity under applied fields, low dielectric losses and high pyroelectric coefficient [10-13]. It was extensively used in electrical devices such as tunable oscillators, microwave phase shifters, delay lines dielectric filters, varactors, multilayer ceramic capacitors, and uncooled infrared focal plane array. However, such applications demand materials having electrical properties, such as, moderate or low permittivity (hundreds), low dielectric losses as well as large tunability. Usually, ferroelectrics are the best tunable materials, but they are characterized also by a very high permittivity. The dielectric properties of ferroelectric ceramics could be significantly modified by doping, by forming solid solutions or composites with other

materials [14-21]. The "dilution" of their dielectric constant and minimization of the dielectric loss of BST-based materials can be achieved by adding amounts of non-ferroelectric dielectrics. However, in this way the tunability is also reduced. By doping BST system with different ions (*e.g.* Ni, Y, Bi, Ga, Mn, Fe etc.), tunability of the resulted compounds can be preserved, whereas their permittivity (ε) value could be reduced [16-21]. In order to obtain the desired characteristics which are not compatible with the pure phase material and to avoid the unwanted chemical reactions that could take place at the interfaces when combining dissimilar materials, the approach to develop porous ceramics was also proposed [22-24]. Usually, porosity is unwanted in microelectronics. However, there are some specific applications where a certain porosity level may be useful, *e.g.* for acoustic impedance adjustment, for permittivity reduction and increase tunability by local field concentration [25,26]. Other use of porous ceramics can be realized by embedding functional groups or other phases into the pores to extend multifunctionality for applications in catalysis and adsorbent supports [27], sensors [28-31], piezoelectric transducers [32] or multiferroic-based multistate memory devices [33,34]. For such applications, microstructural control and achievement of closed porosity are necessary. On the other hand, there is a high interest in the study of porous ceramics for understanding the role of accidental porosity on its own functional properties, which is inherent in any process of sintering.

Porous ceramics with various degrees of porosity and different pore morphologies can be fabricated by incomplete sintering, by direct incorporation of air bubbles or by impregnation of a cellular structure (sponge) with a ceramic suspension, which is further removed by controlled thermal treatments, or by burning different sacrificial templates (or

pore forming agents) with various sizes and shapes during the sintering process. Graphite is known to induce the formation of lamellar porosity tri-dimensionally interconnected. By using a preliminary milling step of the mixed powders (oxide and graphite), an homogeneous pore distribution can be obtained in the bulk ceramics [26,35]. Several other works reported properties of porous ceramics fabricated using different sacrificial templates, such as synthetic organics (stearic acid, polyvinyl butyral - PVB, polyethylene oxide - PEO, polyvinyl chloride - PVC, polymethyl methacrylate - PMMA, sponges), natural organics (tapioca, wheat, starch from corn, rice or potato, glucides, ammonium oxalate monohydrate, dextrin, egg white protein, rice bran powder, etc.), inorganics (carbon black) or liquids (canfene, water solution of Zr and Pb nitrates, Ti isopropoxide and Nb–ammonium complex) as pore forming agents (PFA) [36,37].

The composition $Ba_{0.70}Sr_{0.30}TiO_3$ is ferroelectric at room temperature and presents a ferroelectric to paraelectric phase transition around 35°C, with high dielectric constant and better tunability. The objective of this work was to investigate graphite-derived porous $Ba_{0.70}Sr_{0.30}TiO_3$ ceramics and to evaluate the role of the increasing porosity on the structural, microstructural and functional properties (dielectric and tunability). The experimental dielectric properties were discussed and compared with ones computed from Effective Medium Approximation (EMA) and Finite Element Method (FEM).

2. Experimental details

Porous $Ba_{1-x}Sr_xTiO_3$ (BST) ceramics with composition x=0.3 were prepared by adding 0, 10, 20 and 35% vol. graphite as pore forming agent. BST powders were first

prepared by solid state method from stoichiometric high purity $BaCO_3$ (Merck purity >99%), $SrCO_3$ (Aldrich purity >99.9 %) and TiO_2 (Degussa P25: purity >99.5%) oxide powders according to the reaction:

$$0.7BaCO_3 + 0.3SrCO_3 + TiO_2 \rightarrow Ba_{0.7}Sr_{0.3}TiO_3 + CO_2 \uparrow \quad (1)$$

The powders were mixed and milled by ball-milling for 48h with 5 and 10 mm diameter ZrO_2 milling media and ethanol, then dried at 80°C/72h and manually milled in the agate mortar for de-agglomeration and further sieved (250 µm). The powder mixtures were calcined at 950°C/4h with a heating rate of 150°C/h. The phase formation was investigated as a function of calcination temperature, soaking time and heating/cooling rates. After calcination, the resulted BST powder was planetary milled for 2h in six steps of 20 min at 400 rot/min and 5 pauses of 5 min using 3 mm diameter ZrO_2 balls and ethanol. In order to evaporate ethanol, the milled slurry was placed in rotavapor, then dried and manually re-milled. Graphite powders were wet ball-milled for 48h, using 10 mm diameter Al_2O_3 balls, dried and sieved at 400 µm. The resulted $Ba_{0.7}Sr_{0.3}TiO_3$ powder was mixed for 20 minutes with 0 , 10, 20, 35% vol. graphite. Due to its lamellar structure, the presence of graphite powder tends to induce the formation of cleavage in the graphite-BST powder mixtures during pressing. In order to avoid this phenomenon, the green mix pellets were die-pressed only at 50MPa, while the pure BST powders were die-pressed at 100 MPa in 30 mm diameter dies and then cold-isostatically pressed at 300 MPa.

The sintering of all the green compacts was carried out at 1450°C/2h with a heating step of 100°C/h in a covered Al_2O_3 box. During the sintering, the graphite burned out and resulted CO_2 was eliminated, while the places occupied initially by graphite platelets

became internal micro/macropores distributed in the volume of the ceramic body. After sintering the green compacts, shrinked disc-shaped dense of porous BST samples with various porosities were obtained. To remove the possible stresses due to the sintering and to allow the full reoxidation, the ceramic samples were heated at 1100°C/36h and slowly cooled down to room temperature. The density of the sintered samples was measured by Archimedes method using a density analytical balance and by using dimensional method. The ceramic samples analyzed in this study will be denoted in the following as BST0, BST10, BST20 and BST35, according to the amount of graphite addition.

The phase purity of BST powders and ceramics was checked with a SHIMADZU XRD 6000 diffractometer using Ni-filtered CuKα radiation (λ = 1.5418Å) with scan step increments of 0.02° and counting time of 1s/step, for 2θ ranged between (20÷80)°. The microstructure of BST with different porosity levels was evaluated by scanning electron microscopy (SEM) measurements using FEI Quanta 200 variable pressure-environmental/ESEM.

For the dielectric measurements, Pd-Ag electrodes were deposited on the plane-parallel surfaces of the ceramic pellets. Dielectric measurements were carried out at frequencies of f = (20÷10^6)Hz and temperatures in the range of (25÷200)°C using an RLC type bridge (Agilent E4980A Precision). The high field dielectric measurements were performed by placing the ceramic samples in a cell containing transformer oil. The high voltage was obtained from a function generator coupled with a High-Voltage Amplifier Trek amplifier 30/20A-H-CE (Trek Inc., Medina, NY). In order to obtain accurate tunability data, a circuit which is described in Ref. [38] was used.

3. Results and discussions

3.1. Phase and microstructural characterization

Specific XRD patterns for the $Ba_{0.7}Sr_{0.3}TiO_3$ ceramics with various porosity levels are shown in Fig. 1a. The $Ba_{0.7}Sr_{0.3}TiO_3$ ceramic samples present pure crystalline perovskite phase with the tetragonal symmetry. Since the ferroelectric to paraelectric (tetragonal to cubic) phase transition for this composition is expected around 35°C, the structure at room temperature is most probably tetragonal with a low tetragonality factor c/a close to 1. Rietveld analysis was used to determine the lattice parameters and tetragonality. The indexing of XRD peaks was carried out using the GSAS software suite. The evolution of XRD patterns and lattice parameters (Table 1) revealed that the tetragonal modification is favored for dense structures (see the splitting/asymmetry of the (200) peaks), while at high porosity level, the structure is closer to the cubic one, as also shown by the symmetric shape of the (200) peak (Fig. 1b). It is noticed that the lattice parameter decreases with addition of graphite in the BST ceramics (Table 1). Additionally, it is observed that the intensity of the (200) and (210) peaks are enhanced when increasing the porosity degree, with a slightly shift towards higher 2θ angles. This shift may be due to the decreased inter-atomic spacing of the small BST particles. The increased internal stress in BST particles results in an elastic, compressive volume strain and hence, in a linear strain. This may sometimes lead to a reduced lattice parameter or to interplanar spacing [39]. This also shows that ceramics tend to develop a preferential grain growth at high levels of porosity, which may be attributed to the stress relaxation in the regions adjacent to the pores due to the preferential grain growth [40].

The densities of the sintered BST ceramics as determined by Archimedes method show the maximum relative density of 97% for the pure BST ceramics while after adding graphite pore former at 10, 20 and 35% vol., the resulted relative densities were: 91%, 82% and 71%, respectively. For a better accuracy, we have also checked the density by using dimensional method. The obtained values are: 96.5% for dense BST ceramics, 91.3% for BST10, 82.2% and 67.5% for BST20 and BST35, respectively, similar to ones determined by Archimedes method.

The SEM microstructures of the surface fractures (Fig. 2) allow the observation of grain shape and size, surface morphology, pore size and distribution. A fracture mode transformation from intragranular to intergranular and modifications of the grain size and of the grain boundaries volume are noticed. During the sintering process, progressive microstructural changes appear with the increasing of density. While densification takes place, the pores remain at grain boundaries, and therefore they can be removed or intersect the separation region where grain boundaries can separate from the pores. In this way, some pores can be trapped within grains and a closed porosity is formed. The transgranular fracture reveals a few small and approximately circular intra-granular pores with sizes less than 0.5 μm. This type of intragranular pores which are inherent of any sintering process can be observed in Fig. 2a.

The sum effects of the graphite addition with the sintering temperature are visible in the Figs. 2b, 2c and 2d. Graphite was burned out through the sintering process and this resulted in a modification of morphology, microstructure and pore density of the ceramic product. As expected, the final porosity increases with increasing the amount of graphite. The reducing atmosphere due to the presence of graphite causes a grain growth inhibition

during sintering and limits grain size until sufficiently low levels of porosity or higher driving forces for grain growth are reached. Some pores become intra-granular instead of being inter-granular, mostly when grain boundaries are no longer fixed by pores. After considerable grain growth, closed inter-granular pores are formed. The inter-granular fracture reveals rounded pores of about 15μm diameter, or flat, sometimes lenticular or elongated that are rounded on their grain boundaries facets larger in size (about 120μm). The microstructures of ceramics with high amounts of graphite (Fig. 2c and 2d) show a complex cross-sectional shape of pores along triple lines and substantially elongated pores, mostly oriented to the pressing direction during consolidation step. Graphite has a laminate structure and therefore, the porosity resulting after pyrolysis of graphite is lamellar and horizontally preferentially oriented. Likewise, the sintering anisotropy is attributed to the delamination of the bulk layer caused by the large volume of exit gases formed during the graphite burnout, as it can be observed that pores begin to be interconnected and form visible pore channels in the fracture of samples (Fig. 2c and 2d). The high degree of interconnection of pores shows an open porosity and explains the multilayered structure. As shown in Figs. 2c and 2d, when increasing porosity, the morphology and the distribution of pores can be linked to a multilayered structure. In conclusion, when increasing the graphite amount, a tendency from a closed porosity (BST10) to an interconnected elongated porosity (BST20 and BST35) is observed.

3.2. Low-field effective dielectric properties

3.2.1 Frequency dependence of permittivity and losses

The dielectric properties (real part of permittivity and tangent loss) as a function of frequency at a few selected temperatures for $Ba_{0.7}Sr_{0.3}TiO_3$ ceramics with various porosity levels are summarized in Figs. 3(a-h). All the compositions show a similar trend, irrespective of the porosity degree, with a low-frequency dispersion which is more pronounced when temperature increases (thermally activated phenomenon), characterized by an increase of permittivity and of tangent loss above unity for frequencies below 10^2-10^3 Hz. This frequency dispersion can be assigned to an extrinsic effect (Maxwell-Wagner space charge phenomenon) which is present also in the dense ceramic and is independent on the porosity level. Therefore, this dispersion is not directly related to the air pore-ceramic interfaces, but to local compositional fluctuations (Ba/Sr stoichiometry) inside the ceramic volume. In addition, the presence of small compositional variations (oxygen vacancies) in oxide ceramics sintered at high temperatures is unavoidable, since by sintering of a bulk material it is impossible to fully control the local oxygen stoichiometry [41, 42]. Usually, during cooling from the sintering temperature, the grain boundaries are fully re-oxidized, while the grain bulk still contains a large number of oxygen vacancies. The local inhomogeneity in composition may determine local variations of polarization which lead to uncompensated charge boundaries in the ceramic volume and usually produce an extrinsic polarization denoted as electrostatic space charge or Maxwell-Wagner effect. Due to the mentioned compositional local inhomogeneity, thermally activated low-frequency relaxation due to such slow species gives extrinsic contributions to the permittivity and causes the increase of dielectric losses.

At higher frequencies (above 1kHz), all the ceramics show good dielectric properties, with losses below 3.8% and permittivity values tend to saturate to values that

may be considered as intrinsic. At a fixed frequency (f = 5kHz), the intrinsic permittivity reduces from 7690 (BST0), to 6550 (BST10) and the decrease is more accentuated for high porosity level, to 925 (BST20) and 380 (BST35). The more porous the samples are, a smaller permittivity is determined, as result of a smaller volume of high permittivity material in the ceramic body. However, the decrease is not gradual and is related to the microstructural characteristics of porous samples.

3.2.2 Description of permittivity by finite element model and effective field approximation

In order to describe the role of porosity level and of the microstructures on the dielectric properties, two theoretical approaches have been used: effective medium approximation (EMA) and finite element method (FEM). By considering the microstructural features of the porous ceramics, several types of microstructures have been simulated and the permittivity was evaluated and compared with the experimental data (Fig. 4): (i) columnar structures with cylindrical pores, (ii) 0-3 connectivity with spherical pores perfectly isolated into the ceramic matrix and (iii) layered structures. All the microstructures have been treated as composites, with bulk BST regions and pores as "phases", and the corresponding numerical values $\varepsilon_{bulk} = 8000$ and $\varepsilon_{pores} = 1$ have been employed in calculations. The numerical value assigned to the dense regions is slightly higher than the permittivity of the sample with the highest permittivity BST0 due to the fact that the dense ceramic has a porosity of about 3%. This value was estimated by considering that at small porosity pores are isolated (0-3 connectivity) and the dependences of the

effective permittivity on porosity can be described by Maxwell-Garnett law, as it will be described in the following.

Generally, for all types of composites the effective permittivity is computed as the ratio between the average electric displacement and the average local electric field $\langle E_{local} \rangle$:

$$\varepsilon_{eff} = \frac{\langle \varepsilon_{local} E_{local} \rangle}{\langle E_{local} \rangle}, \quad (2)$$

The first configuration chosen for comparison contains columnar structures with cylindrical pores oriented parallel to the direction of the applied field (Fig. 4a). In this case, the bulk/air interfaces do not produce any distortion of the local fields because they are tangential to the field directions. Therefore, starting from Eq. (2) the effective permittivity dependence on the porosity is obtained as:

$$\varepsilon_{eff} = p \cdot \varepsilon_{pores} + (1-p) \cdot \varepsilon_{bulk}, \quad (3)$$

where p is the porosity. As observed in Fig. 4, this dependence proves to overestimate the effective permittivity for all the BST porous samples, which means that this type of microstructure is very far from the real microstructures.

The second configuration is represented by 0-3 connectivity with spherical pores perfectly isolated (Fig. 4b). Accordingly to the Lorentz sphere problem, the average field inside pores is $\langle E_{pores} \rangle = 3\varepsilon_{bulk} / (\varepsilon_{pores} + 2\varepsilon_{bulk}) \cdot \langle E_{bulk} \rangle$, wherefrom, using Eq. (2), the dependence of the effective permittivity on porosity is (parallel capacitor connection):

$$\varepsilon_{eff} = \varepsilon_{bulk} + 3p\varepsilon_{bulk} \frac{\varepsilon_{pores} - \varepsilon_{bulk}}{\varepsilon_{pores} + 2\varepsilon_{bulk} - p \cdot (\varepsilon_{pores} - \varepsilon_{bulk})}. \quad (4)$$

Eq. (4) is known as Maxwell-Garnett's equation and is applicable for structures with 0-3 connectivity [45]. The numerical value of ε_{bulk} was chosen in such a way that the permittivity of the sample at 3% porosity is ~7690, as in experiment for BST0. The Maxwell-Garnett equation describes quite satisfactory the permittivity of the sample BST10 with 9% porosity (~6900 in calculation and 6550 in experiment). This result confirms the SEM observations of BST10 ceramic (Fig. 2b), which has a microstructure close to the one assumed by the Maxwell-Garnett approximation: spherical and closed pores (0-3). However, this equation does not succeed to describe the samples with higher porosity levels, which have a predominant elongated porosity.

The third configuration chosen for computing the effective permittivity contains layered structures (successive bulk and air layers, *i.e.* (2-2) connectivity) (Fig. 4c-4d). This type of configuration was employed only to prove the possibility of obtaining extremely low permittivity in such particular cases, although it is impossible to produce experimentally real samples with such types of porosity due to mechanical reasons. In this case the relation between the local field on the two components is found from the boundary condition concerning the electrical displacement at the ceramic-pore interfaces: $\varepsilon_{pores}E_{pores} = \varepsilon_{bulk}E_{bulk}$, where it can be shown that the $\varepsilon_{eff}(p)$ dependence is given from the equation (series capacitor connection):

$$\frac{1}{\varepsilon_{eff}} = \frac{p}{\varepsilon_{pores}} + \frac{1-p}{\varepsilon_{bulk}} \qquad (5)$$

As observed in Fig. 4, the effective permittivity described by a layered structure is strongly underestimated for all the porous samples. However, this type of microstructure explains, at least as trends, the reasons for such a low permittivity obtained for the samples

BST20 and BST35 (925 and 380, respectively). The low permittivity values are related to the lamellar shape of the pore forming agents (graphite), which tends to orient perpendicular to the pressing direction during forming (the same as the direction of the applied field in the electrical measurements). Therefore, the real microstructure of the samples BST20 and BST35 represent in fact combinations between the second configuration and the third configuration. Such microstructures cannot be resolved by EMA models and FEM calculations are necessary.

In order to describe the properties of these types of complex porous samples, different virtual systems with pores of flat ellipsoidal shapes in randomly generated positions were generated and analyzed. These pores have a much smaller size on vertical axis than in the perpendicular plan to the field direction (Fig. 4d). By comparisons with the other configurations for which EMA models still could be applied with a certain approximation, this complex case describing the realistic microstructures (Fig. 2c-2d) cannot be described by analytical formulas and for this reason, 3D Finite Element Method (FEM) has been employed. In the FEM procedures the Laplace equation ($\nabla \cdot (\varepsilon \nabla V) = 0$, where ε is the local permittivity and V is the local potential) is solved, taking into account the boundary conditions in a parallel-plate capacitor: Dirichlet boundary conditions on the top and bottom surfaces and Neumann boundary conditions at lateral surfaces, as described in detail elsewhere [46,47]. After computing the local potentials and the local electric fields, the average electric displacement and the average electric field were estimated and the effective permittivity was derived from the Eq. (2). Using this method, different simulations were performed at different porosity levels in the range from 0% to 30% and the dependence of the computed effective permittivity on the porosity for this type of

microstructure is represented in Fig. 4. This method succeeds to explain the dielectric properties of the samples with 18% and 29% porosity levels (BST20 and BST35, respectively) in relation with the observed microstructural features: the lower permittivity is related to the narrow pores oriented perpendicular on the applied field direction, similar to the case of the layered structures.

To summarize this paragraph, the effective field approach shows that the present porous ceramics cannot be described by a single type of EMA configuration. Their effective permittivity shows a strong depression when increasing the porosity level. Besides the role of porosity volume, a major role is played by the modification of the microstructural features, from (0-3) connectivity (closed porosity) in the case of BST0 and BST10, to layered-like structures for high porosity levels in BST20 and BST35.

3.2.3 Temperature dependence of permittivity and Curie-Weiss analysis

The temperature dependence of permittivity at a fixed frequency f=100 kHz (Fig. 5a) shows a maximum corresponding to the ferroelectric to paraelectric phase transition with a Curie temperature close to room temperature (around 35°C), irrespective of the porosity volume. The porosity level does not modify the temperature corresponding to the permittivity maximum. However, since the ferroelectric phase content has been reduced by the presence of air pores, it is expected also a lower dielectric permittivity for high porosity content. According to the Curie Weiss law $\varepsilon=C/(T-T_0)$ in which the Curie constant C and Curie-Weiss temperature T_0 can be determined by linear regression analysis from the reciprocal permittivity *vs.* temperature dependence (Fig. 5b), it is observed that the slope increases at increasing porosity, *i.e.* the Curie constant, indicating the ferroelectricity

strength, decreases (Table 2). Additionally, the Curie-Weiss temperature (T_0) gradually shifts to lower values when increasing the porosity level. The reduction of both Curie-Weiss temperature and Curie constant with increasing porosity are explained by the di-phase composite character of the porous ceramics, which is formed by high permittivity ferroelectric ceramic and air pores (ε_r=1).

In conclusion, the low-field dielectric properties are fully explained in correlation with the microstructural characteristics of the present ceramic samples: the intrinsic permittivity reduces at increasing addition of graphite pore forming agent, as a consequence of the "sum property" [43,44], which represents a weighted sum of the contributions of the individual component phases in the ceramic-air composite, proportional to the weight/volume fractions of the phases. Similar results, concerning the influence of porosity on the dielectric and tunability properties, were reported for porous $Ba_{0.60}Sr_{0.40}TiO_3$ and $Ba_{0.67}Sr_{0.33}TiO_3$ ceramics [23,48]. It is worth to mention that the resulted permittivity is not only dependent on the air pore/ceramic volumic ratio and the permittivity of the dense BST composition, but also is a consequence of the phase interconnectivity, which changes from a 0-3 for small porosity to a combined 0-3 with 2-2 connectivity for high porosity amount.

3.3 High field dielectric properties (tunability)

The field dependences of the dielectric constant and relative dc-tunability of the $Ba_{0.70}Sr_{0.30}TiO_3$ ceramics with various porosities were determined at room temperature at increasing/decreasing dc-fields and they are presented in Figs. 6a-b. A strong nonlinearity was observed for all the ceramics, with a tendency toward saturation for high fields (higher than 2.5 kV/mm for BST0, BST20 and BST35), while the sample BST10 did not sustain

the application of fields higher than 1kV/mm, most probable due to some internal defects. However, at low fields, the nonlinear behavior is present in this sample and the relative tunability value is about 0.17 for an applied field of 0.85kV/mm, comparable to those obtained for the other investigated ceramics (Fig. 6b). Irrespective of the porosity level, the $\varepsilon(E)$ dependencies show a non-hysteretic behavior, due to the proximity of ferroelectric to paraelectric phase transition of the $Ba_{0.70}Sr_{0.30}TiO_3$ composition at room temperature [49]. For a given value of the applied field E=2.3kV/mm, the relative tunability n_{rel} keeps similar values, irrespective of porosity level, ranging between 0.41 for BST35 and 0.44 for BST0 (Fig. 6b). The tunability values are comparable with ones reported in literature for similar ceramic compositions [50, 51]. These experimental results confirm the results of previous FEM calculations [46], which demonstrated that elongated porosity may be favorable for tunability, due to the concentration of high fields in ferroelectric regions adjacent to the ceramic-air pore interfaces. Although the amount of active material (ferroelectric) causing dielectric non-linearity reduces when increasing porosity, the remained ferroelectric regions are subjected to a much higher fields than in the dense material and an overall high tunability is still maintained.

4. Conclusions

The role of porosity level of $Ba_{0.70}Sr_{0.30}TiO_3$ ceramics on the structural, microstructures and electrical properties was investigated. Pure tetragonal perovskite phase was found in all the ceramics, with a decreasing tetragonality factor towards a cubic structure when increasing porosity level. A strong decrease of the effective permittivity when increasing porosity was found, as a consequence of both the increasing amount of air

pores and of the modification of pore interconnectivity from a (0-3) towards a complex structure with flat porosity. The obtained results were compared with ones computed within effective field approximations and finite element calculations. It was found that Maxwell-Garnett formula well describes the properties of ceramics with small porosity only, while for high porosity level the complex interconnected porosity which can be described as combinations between (0-3) and (2-2) connectivity, the dielectric properties can be described correctly by numerical FEM calculations only. The relative tunability of porous BST structures preserved similar values as in the dense ceramics, irrespective of the porosity level. Therefore, in porous ceramics the permittivity can be reduced down to a few hundreds, without losing the high tunability. Although the application of porous structures in tunable devices may pose some technological limitations, the idea to design porous ferroelectric microstructures with strong non-linear dielectric character based on the field lines concentration due to the boundary conditions at the ferroelectric-air pore interfaces deserves a further attention.

Acknowledgements: This work was financially supported by CNCS-UEFISCDI project PNII-RU-TE-2012-3-0150. The first author acknowledges the strategic grant POSDRU/159/1.5/S/137750, Project "Doctoral and Postdoctoral programs support for increased competitiveness in Exact Sciences research" co-financed by the European Social Fund within the Sectorial Operational Program Human Resources Development 2007 – 2013. The authors are grateful to dr. Mirela Airimioaei for the structural calculations.

References

[1] F. Jona, G. Shirane, Ferroelectric crystals, Dover Publications, INC., New York, 1993.

[2] T. Wang, L. Jin, L. Shu, Q. Hu, X. Wei, Energy storage properties in $Ba_{0.4}Sr_{0.6}TiO_3$ ceramics with addition of semi-conductive $BaO–B_2O_3–SiO_2–Na_2CO_3–K_2CO_3$ glass, J. Alloys Comp. 617 (2014) 399–403.

[3] C. Miot, C. Proust, E. Husson, Dense ceramics of $BaTiO_3$ produced from powders prepared by a chemical process, J. Eur. Ceram. Soc. 15 (1995) 1163-1170.

[4] J. Li, H. Kakemoto, S. Wada, T. Tsurumi, H. Kawaji, Dielectric relaxation in gigahertz region and phase transition of $BaTiO_3$ – based ceramics, J. Appl. Phys. 100 (2006) 024106.

[5] M.L.V. Mahesh, V.V. Bhanu Prasad, A.R. James, Enhanced dielectric and ferroelectric properties of lead-free $Ba(Zr_{0.15}Ti_{0.85})O_3$ ceramics compacted by cold isostatic pressing, J. Alloys Comp. 611 (2014) 43-49.

[6] M.T. Buscaglia, M. Bassoli, V. Buscaglia, R. Vormberg, Solid-state synthesis of nanocrystalline $BaTiO_3$: reaction kinetics and powder properties; J. Amer. Ceram. Soc. 91 (2008) 2862–2869.

[7] Z. Zhe, V. Buscaglia, M. Viviani, M.T. Buscaglia, L. Mitoseriu, A. Testino, M. Nygren, M. Johnsson, P. Nanni, Grain-size effects on the ferroelectric behavior of dense nanocrystalline $BaTiO_3$ ceramics, Phys. Rev. B 70 (2004) 024107.

[8] L. Curecheriu, S.B. Balmus, M.T. Buscaglia, V. Buscaglia, A. Ianculescu, L. Mitoseriu, Grain size-dependent properties of dense nanocrystalline barium titanate ceramics, J. Am. Ceram. Soc. 95 (2012) 3912–3921.

[9] S. Liu, V.Y. Zenou, I. Sus, T. Kotani, M. van Schilfgaarde, N. Newman, Structure–dielectric property relationship for vanadium - and scandium-doped barium strontium titanate, Acta Mater. 55 (2007) 2647–2657.

[10] T. Hungria, M. Alguero, A.B. Hungria, A. Castro, Dense fine-grained $Ba_{1-x}Sr_xTiO_3$ ceramics prepared by the combination of mechanosynthesized nanopowders and spark plasma sintering, Chem. Mater. 17 (2005) 6205–6212.

[11] C. Mao, S. Yan, S. Cao, C. Yao, F. Cao, G. Wang, X. Dong, C. Yang, Effect of grain size on phase transition, dielectric and pyroelectric properties of BST ceramics, J. Eur. Ceram. Soc. 34 (2014) 2933–2939.

[12] J. Zhang, J. Zhai, X. Chou, J. Shao, X. Lu, X. Yao, Microwave and infrared dielectric response of tunable $Ba_{1-x}Sr_xTiO_3$ ceramics, Acta Mater 57 (2009) 4491–4499.

[13] Y. Yu, X. Wang, X. Yao, Dielectric properties of $Ba_{1-x}Sr_xTiO_3$ ceramics prepared by microwave sintering, Ceram. Int. 39 (2013) S335–S339.

[14] I. Norezan, A.K. Yahya, M.K. Talari, Effect of $(Ba_{0.6}Sr_{0.4})TiO_3$ (BST) Doping on dielectric properties of $CaCu_3Ti_4O_{12}$ (CCTO), J. Mater. Sci. Technol. 28 (2012) 1137–1144.

[15] Y.S. Ham, J.H. Koh, Impedance spectroscopy of Li_2CO_3 doped $(Ba,Sr)TiO_3$ ceramic, Sol. State Sci. 16 (2013) 53–56.

[16] X. Wang, W. Lu, J. Liu, Y. Zhou, D. Zhou, Effects of La_2O_3 additions on properties of $Ba_{0.6}Sr_{0.4}TiO_3$–MgO ceramics for phase shifter applications, J. Eur. Ceram. Soc. 26 (2006) 1981–1985.

[17] L.X. Zhang, W. Chen, X. Ren, Large recoverable electrostrain in Mn-doped $(Ba,Sr)TiO_3$ ceramics, Appl. Phys. Lett. 85 (2004) 5658–5660.

[18] L. Tang, J. Wang, J. Zhai, L.B. Kong, X. Yao, Controllable-permittivity and high-tunability of $Ba_{0.5}Sr_{0.5}TiO_3$/MgO based ceramics by composite configuration, Appl. Phys. Lett. 102 (2013) 142907.

[19] R.H. Liang, X.L. Dong, Y. Chen, F. Cao, Y.L. Wang, Effect of La_2O_3 doping on the tunable and dielectric properties of BST/MgO composite for microwave tunable application, Mater. Chem. Phys. 95 (2006) 222–228.

[20] J. Chen, La doping effect on the dielectric property of barium strontium titanate glass ceramics, J. Mater. Sci. Technol. 30 (2014) 295-298.

[21] C. Liu, P. Liu, G.G. Yao, X.B. Bian, H.X. Jing, X.G. Lu, C.J. Gao, Improvement of dielectric thermal stability of BST ferroelectric material for tunable applications, Mater. Res. Bull. 46 (2011) 1510–1514.

[22] I. Nettleship, Applications of porous ceramics, Key Eng. Mater. 122-124, (1996) 305-324.

[23] Y. Zhang, Electric field-dependent dielectric properties and high tunability of porous $Ba_{0.5}Sr_{0.5}TiO_3$ Ceramics, J. Am. Ceram. Soc. 90 (2007) 1327–1330.

[24] S. Geis, P. Lobmann, S. Seifert, J. Fricke, Dielectric properties of PZT aerogels, Ferroelectrics 241, (2000) 1719-1726.

[25] D. Piazza, C. Galassi, A. Barzegar, D. Damjanovic, Dielectric and piezoelectric properties of PZT ceramics with anisotropic porosity, J. Electroceram. 24 (2010) 170–176.

[26] C.E. Ciomaga, L. Padurariu, L.P. Curecheriu, N. Lupu, I. Lisiecki, M. Deluca, S. Tascu, C. Galassi, L. Mitoseriu, Using multi-walled carbon nanotubes in spark plasma sintered Pb(Zr0.47Ti0.53)O3 ceramics for tailoring dielectric and tunability properties, J. Appl. Phys. 116, 164110 (2014)

[27] A. Julbe, D. Farrusseng, C. Guizard, Porous ceramic membranes for catalytic reactors — overview and new ideas, J. Membrane Sci. 181 (2001) 3-20.

[28] C.M.A. Parlett, K. Wilson, A.F. Lee, Hierarchical porous materials: catalytic applications, Chem. Soc. Rev. 42 (2013) 3876-3893.

[29] K.S. Chou, T.K. Lee, F.J. Liu, Sensing mechanism of a porous ceramic as humidity sensor, Sens. & Act. B 56 (1999) 106–111.

[30] E.S. Gomez, Porous Ferroelectric Ceramic as Gas Sensor Based on BaTiO3/SiO2 , Ferroelectrics 445 (2013) 88-95.

[31] R. Farahani, R. Wagiran, M.N. Hamidon, Humidity Sensors Principle, Mechanism, and Fabrication Technologies: A Comprehensive Review, Sensors 14 (2014) 7881–7939.

[32] F. Levassort, J. Holc, E. Ringgaard, T. Bove, M. Kosec, M. Lethiecq, Fabrication, modelling and use of porous ceramics for ultrasonic transducer applications, J. Electroceram. 19 (2007) 125–137.

[33] H.C. Nie, N.B. Feng, X.F. Chen, G.S. Wang, X.L. Dong, Y. Gu, H.L. He, Y. Sheng, Enhanced ferroelectric properties of intragranular-porous $Pb(Zr_{0.95}Ti_{0.05})O_3$ ceramic fabricated with carbon nanotubes, J. Amer. Ceram. Soc. 93 (2010) 642–645.

[34] P. Ferreira, R.Z. Hou, A. Wu, M.G. Willinger, P.M. Vilarinho, J. Mosa, C. Laberty-Robert, C. Boissiere, D. Grosso, C. Sanchez, Nanoporous piezo- and ferroelectric thin films, Langmuir 28(5) (2012) 2944-2949.

[35] T. Ohji, M. Fukushima, Macro-porous ceramics: processing and properties, Int. Mater. Rev. 57 (2012) 115-131.

[36] E. Mercadelli, A. Sanson, C. Galassi, Porous piezoelectric ceramics, in: E. Suaste-Gomez (Ed.), Piezoelectric Ceramics, Sciyo, 2010, pp. 111-128.

[37] E. Mercadelli, A. Sanson, P. Pinasco, E. Roncari, C. Galassi, Tape cast porosity graded piezoelectric ceramics, J. Eur. Ceram. Soc. 30 (2010) 1461-1467.

[38] F.M. Tufescu, L. Curecheriu, A. Ianculescu, C.E. Ciomaga, L. Mitoseriu, High-voltage tunability measurements of the $BaZr_xTi_{1-x}O_3$ ferroelectric ceramics, J. Optoelectron. Adv. Mater. 10(7) (2008) 1894–1897.

[39] K. Verma, S. Sharma, D.K. Sharma, R. Kumar, R. Rai, Sol-gel processing and characterization of nanometersized $(Ba,Sr)TiO_3$ ceramics, Adv. Mat. Lett. 3(1) (2012) 44-49.

[40] C. Mao, S. Yan, S. Cao, C. Yao, F. Cao, G. Wang, X. Dong, X. Hu, C. Yang, Effect of grain size on phase transition, dielectric and pyroelectric properties of BST ceramics, J. Eur. Ceram. Soc. 34 (2014) 2933–2939.

[41] A Pelaiz-Barranco, J.D.S Guerra, R. Lopez-Noda, E.B Araujo, Ionized oxygen vacancy-related electrical conductivity in $(Pb_{1-x}La_x)(Zr_{0.90}Ti_{0.10})_{1-x/4}O_3$ ceramics, J. Phys. D: Appl. Phys. 41 (2008) 215503-5.

[42] C.E. Ciomaga, M.T. Buscaglia, V. Buscaglia, L. Mitoseriu, Oxygen deficiency and grain boundary-related giant relaxation in $Ba(Zr,Ti)O_3$ ceramics, J. Appl. Phys. 110 (2011) 114110-7.

[43] J. Van Suchtelen, Product properties: A new application of composite materials, Philips Res. Rep., 27, 28 (1972).

[44] L. Mitoseriu, V. Buscaglia, Intrinsic/extrinsic interplay contributions to the functional properties of ferroelectric-magnetic composites", Phase Trans. 79 (2006) 1–27.

[45] C.E. Ciomaga, C.S. Olariu, L. Padurariu, A.V. Sandu, C. Galassi, L. Mitoseriu, Low field permittivity of ferroelectric-ferrite ceramic composites. Experiment and Modeling J. Appl. Phys. 112(9) (2012) 094103-7.

[46] L. Padurariu, L. Curecheriu, C. Galassi, L. Mitoseriu, Tailoring non-linear dielectric properties by local field engineering in anisotropic porous ferroelectric structures, Appl. Phys. Lett. 100 (2012) 252905-5.

[47] C.S. Olariu, L. Padurariu, R. Stanculescu, C. Baldisserri, C. Galassi, L. Mitoseriu, Investigation of low field dielectric properties of anisotropic porous Pb(Zr,Ti)O_3 ceramics: Experiment and modeling, J. Appl. Phys. 114 (2013) 214101-10.

[48] Y. Zhang, G. Wang, K. Wang, Y. Wang, X. Dong, The model of electric field dependent dielectric properties for porous ceramics, J. Appl. Phys. 103 (2008) 114103-5.

[49] G. Dong, S. Ma, J. Du, J. Cui, Dielectric properties and energy storage density in ZnO-doped $Ba_{0.3}Sr_{0.7}TiO_3$ ceramics, Ceram. Int. 35 (2009) 2069–2075.

[50] L.P. Curecheriu, L. Mitoseriu, A. Ianculescu, Nonlinear dielectric properties of $Ba_{1-x}Sr_xTiO_3$ ceramics, J. Alloys Comp. 482 (2009) 1–4.

[51] C. Liu, P. Liu, Microstructure and dielectric properties of BST ceramics derived from high-energy ball-milling, J. Alloys Comp. 584 (2014) 114–118.

Figure Captions

Fig. 1. XRD patterns of $Ba_{0.7}Sr_{0.3}TiO_3$ ceramics with different porosity levels (a) and detailed representation in the range of 2theta from 45 to 48 degree (b).

Fig. 2. Microstructures of BST ceramics with progressive porosity increase: a) dense BST ceramic sample (BST0); b) BST10 (BST with 10 vol.% graphite); c) BST20 (BST with 20 vol.% graphite); d) BST35 (BST with 35 vol.% graphite).

Fig. 3. Frequency dependence of permittivity and tangent loss for: (a-b) dense BST ceramic (BST0); (c-d) BST10 (BST with 10 vol.% graphite); (e-f) BST20 (BST with 20 vol.% graphite); (g-h) BST35 (BST with 35 vol.% graphite).

Fig. 4. Effective permittivity *vs.* porosity level, computed for different configurations: (a) columnar porosity, (b) closed spherical pores (0-3 connectivity), (c) layered structures (2-2) and (d) structures with lamellar porosity. In the microstructural images: dark - bulk regions, gray – pores.

Fig. 5. Temperature dependences of the real part of permittivity (a) and Curie-Weiss analysis (b) for $Ba_{0.7}Sr_{0.3}TiO_3$ ceramics with different porosity levels.

Fig. 6. Electric field dependence of the dielectric constant (a) and field-dependence of the corresponding relative tunability (b) for all investigated ceramics with different porosity levels.

Table Captions

Table 1. Lattice parameter of the BST investigated samples, from Rietveld refinement.

Table 2. Computed Curie Weiss temperature and Curie constant for $Ba_{0.7}Sr_{0.3}TiO_3$ ceramics with different porosities.

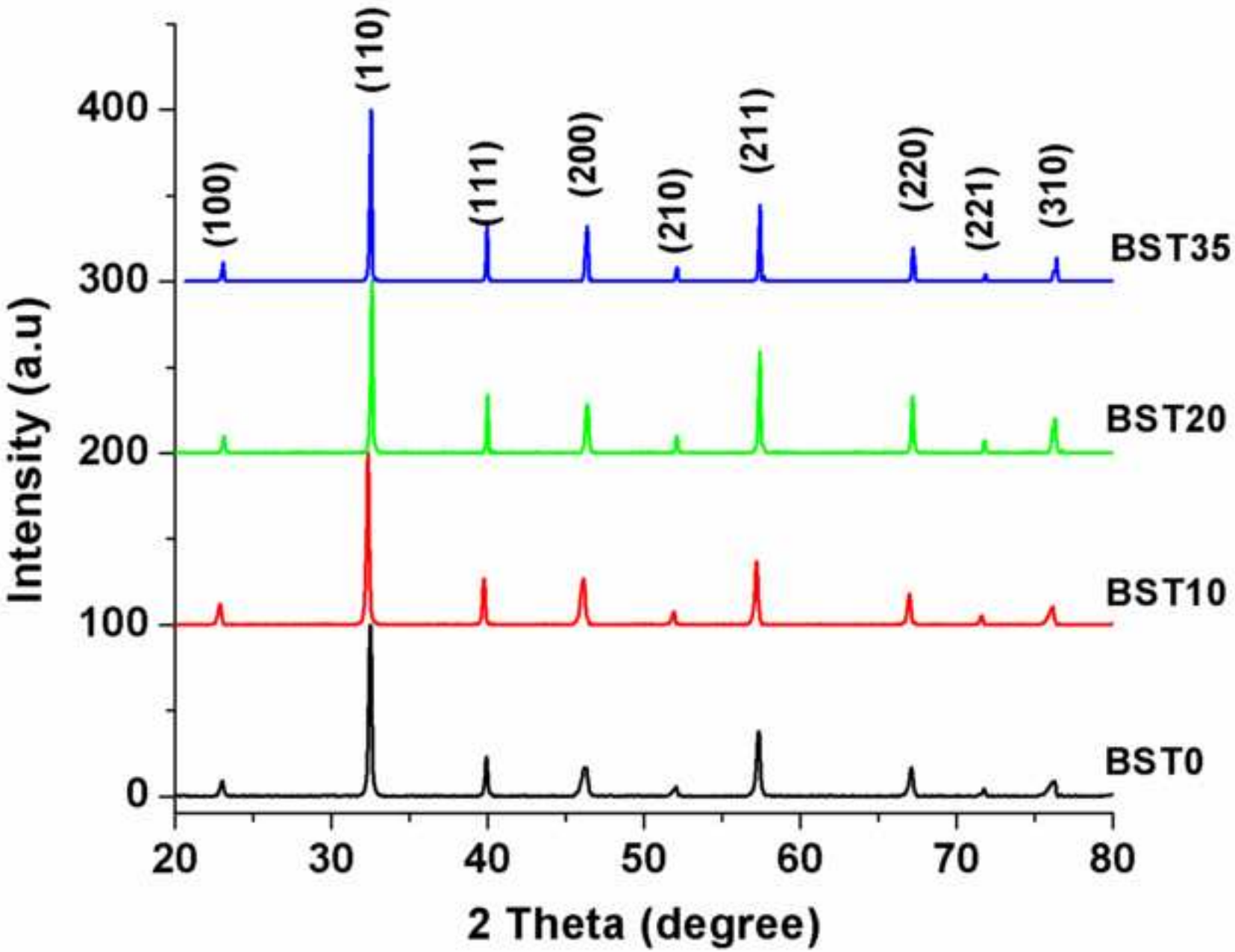

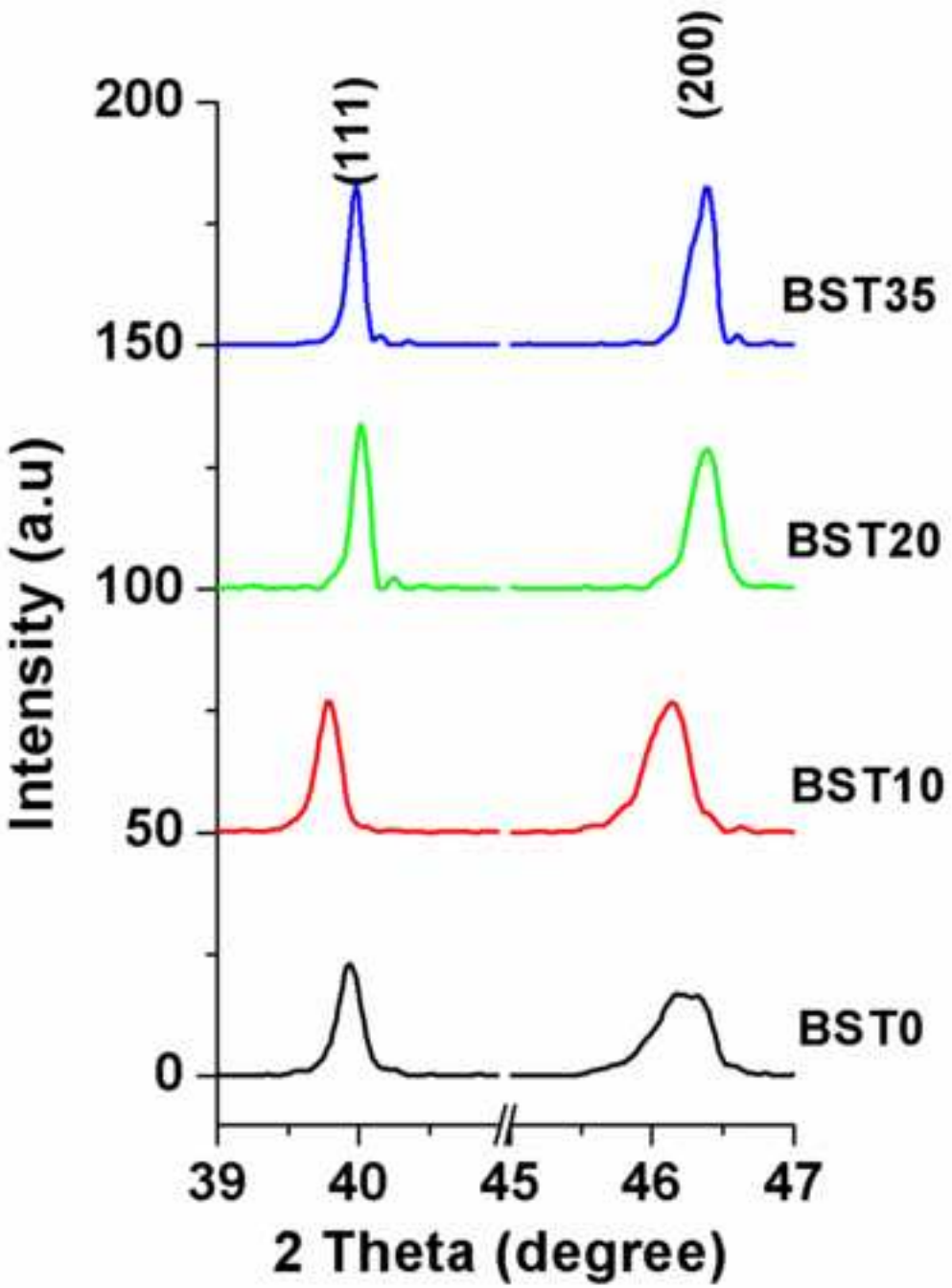
(111)
(200)
BST35
BST20
BST10
BST0
Intensity (a.u)
200
150
100
50
0
39
40
45
46
47
2 Theta (degree)

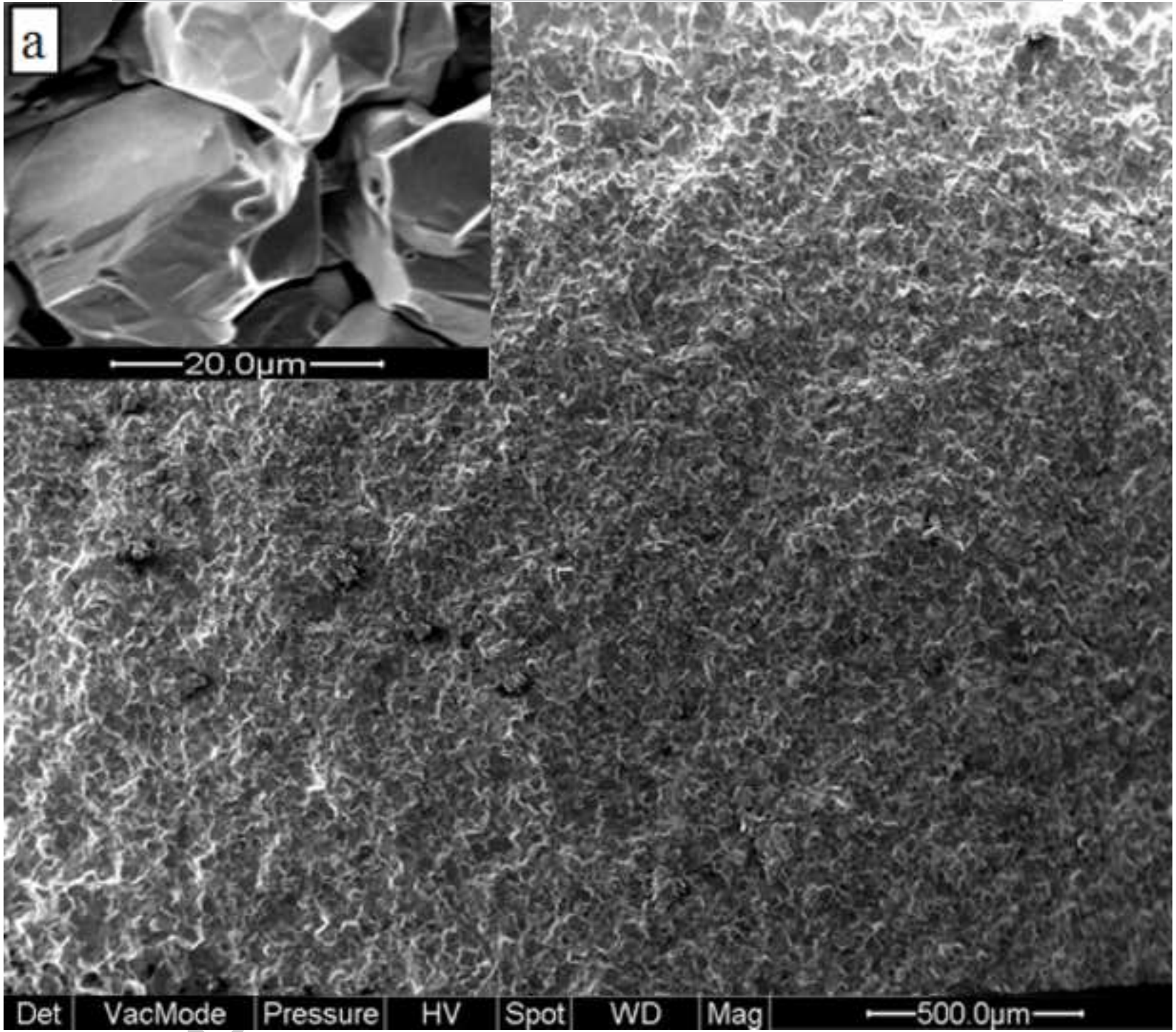

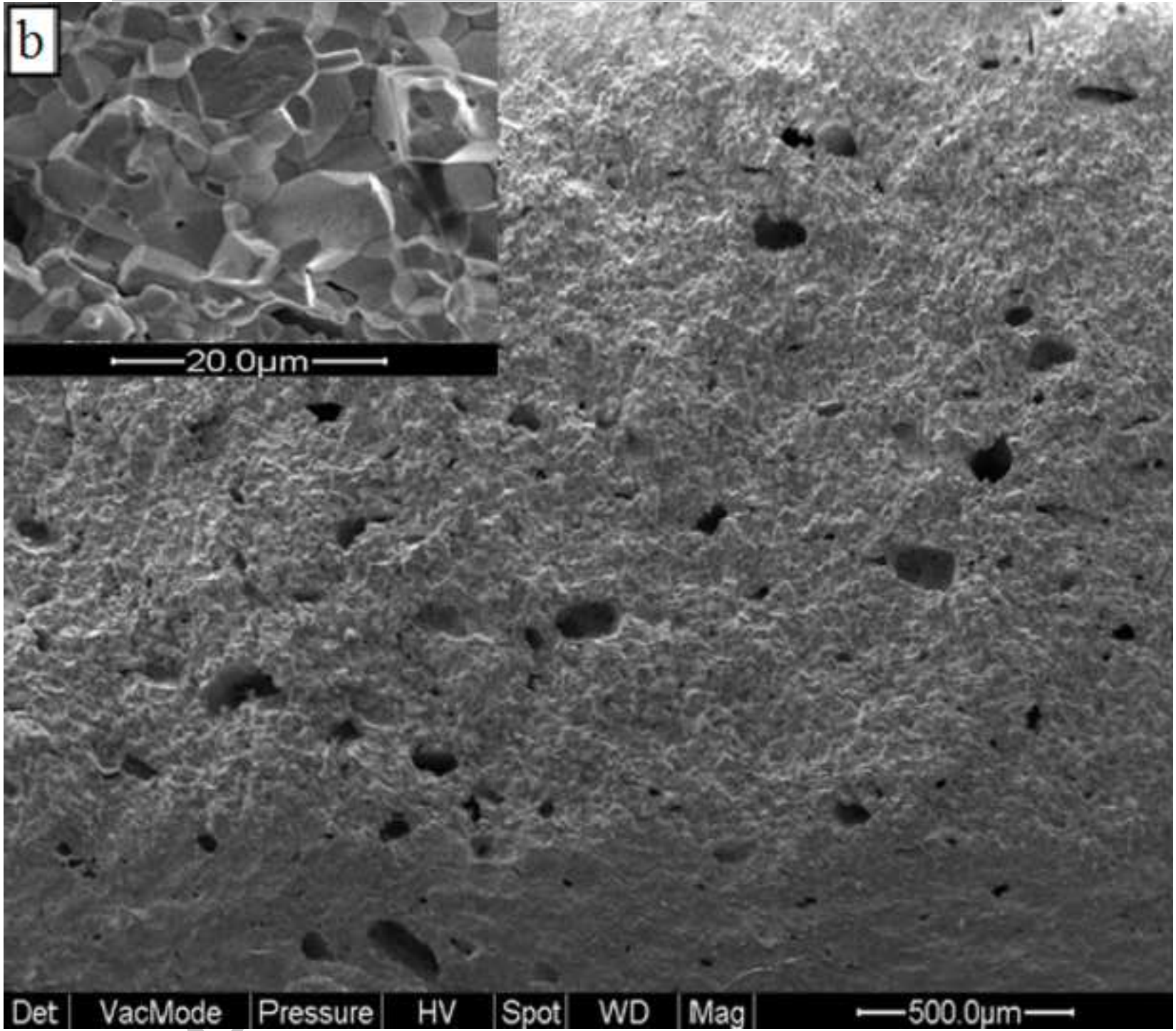

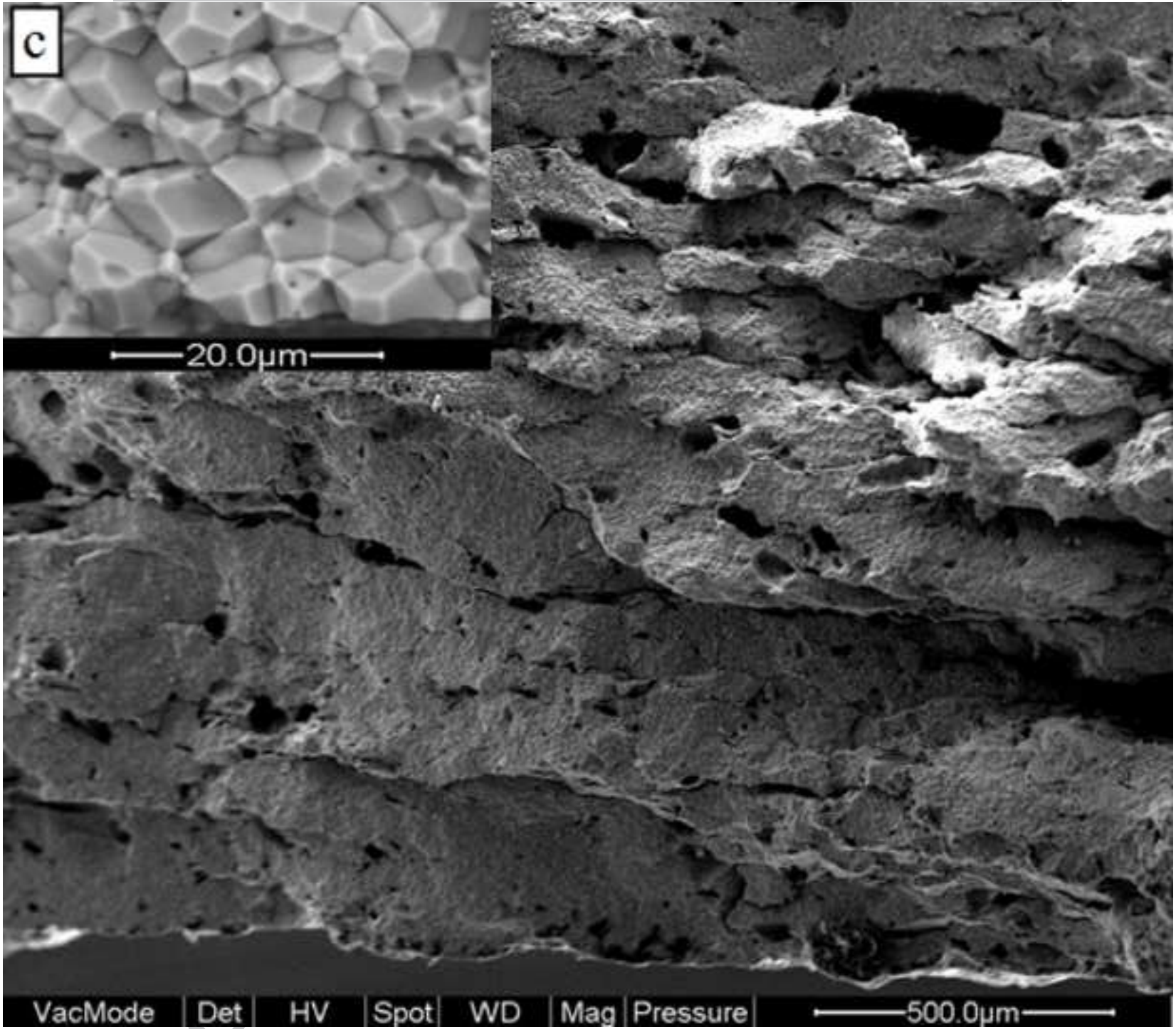

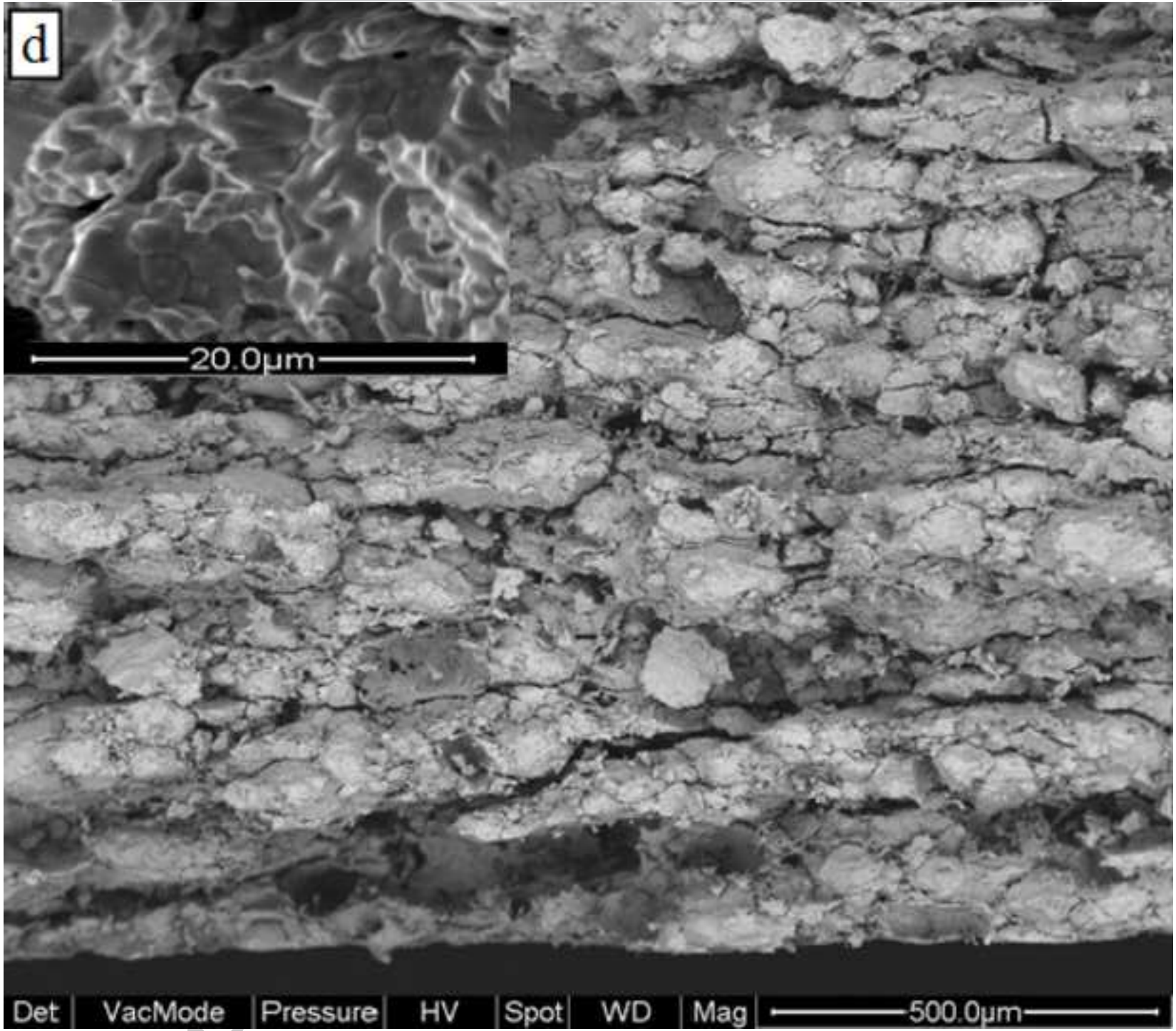

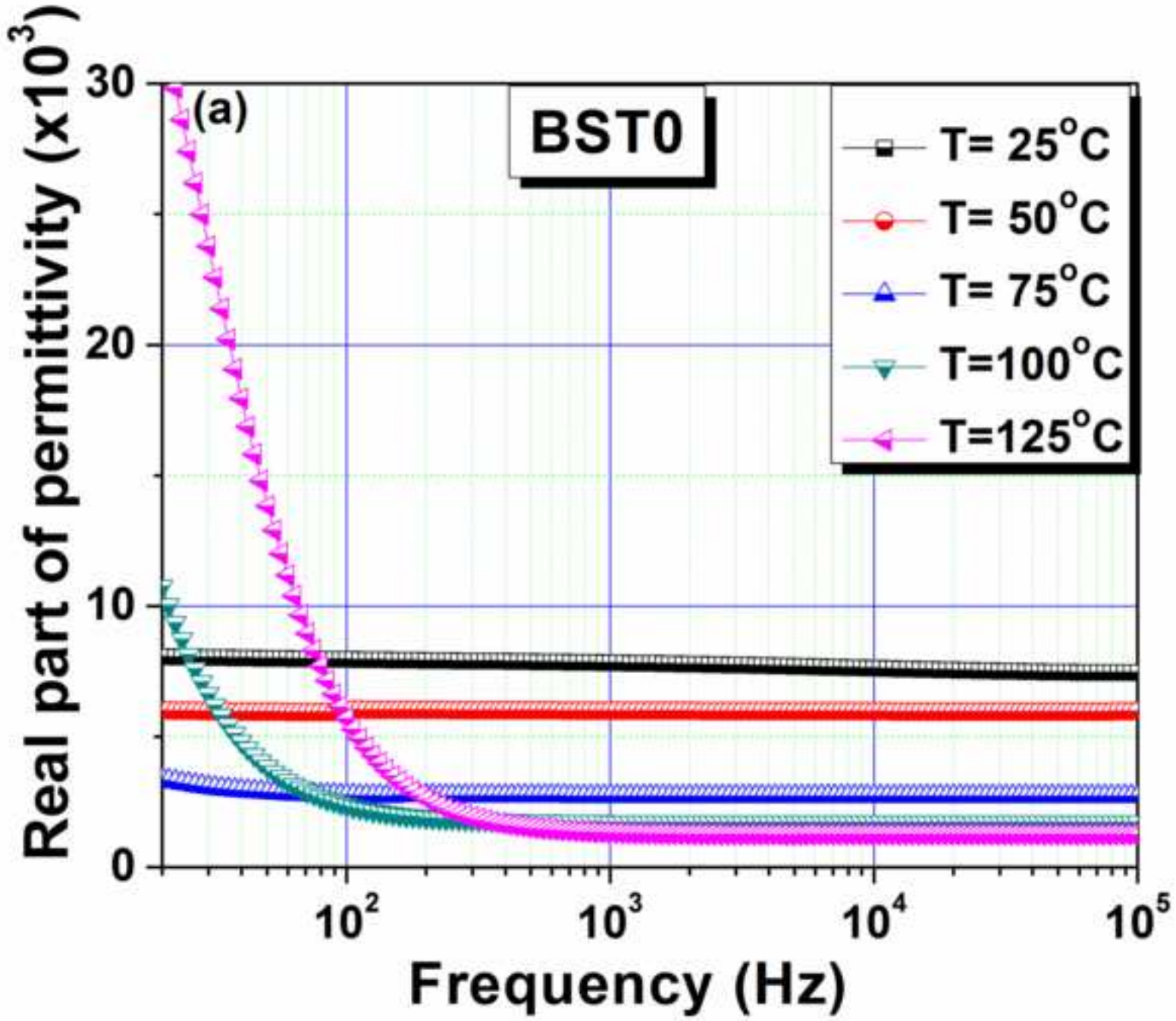

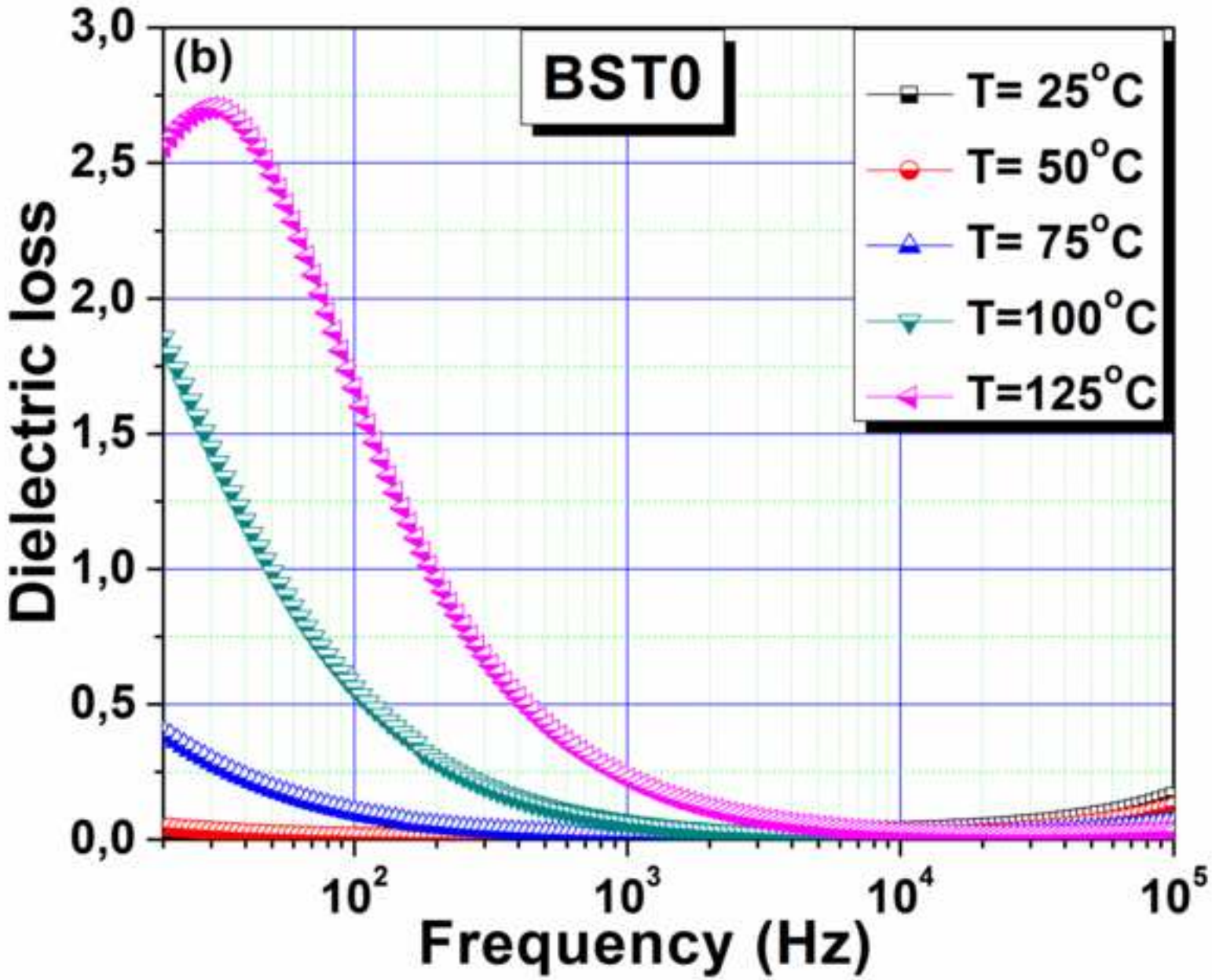
(b)
BST0
T= 25°C
T= 50°C
T= 75°C
T=100°C
T=125°C
Dielectric loss
3,0
2,5
2,0
1,5
1,0
0,5
0,0
10^2
10^3
10^4
10^5
Frequency (Hz)

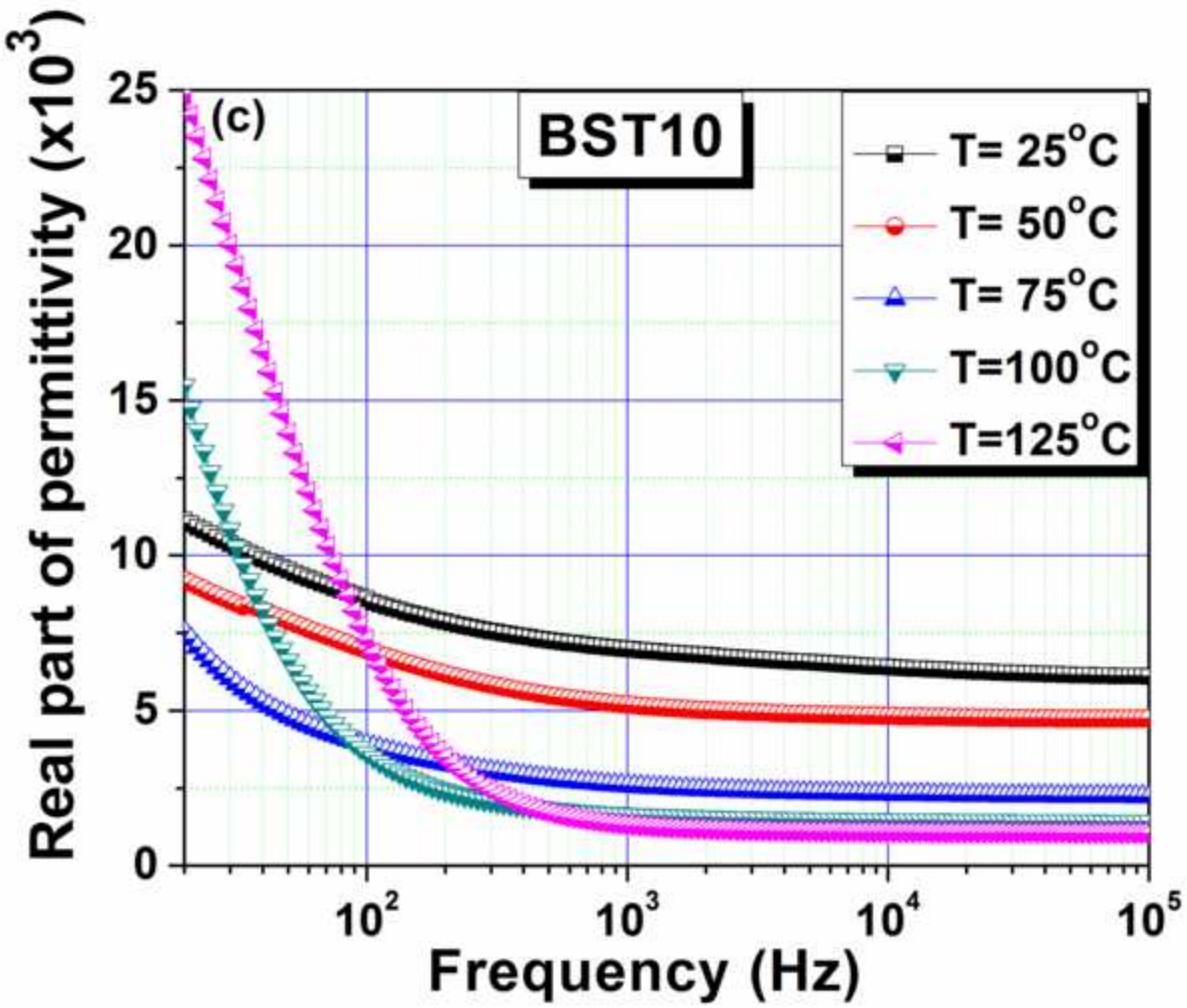

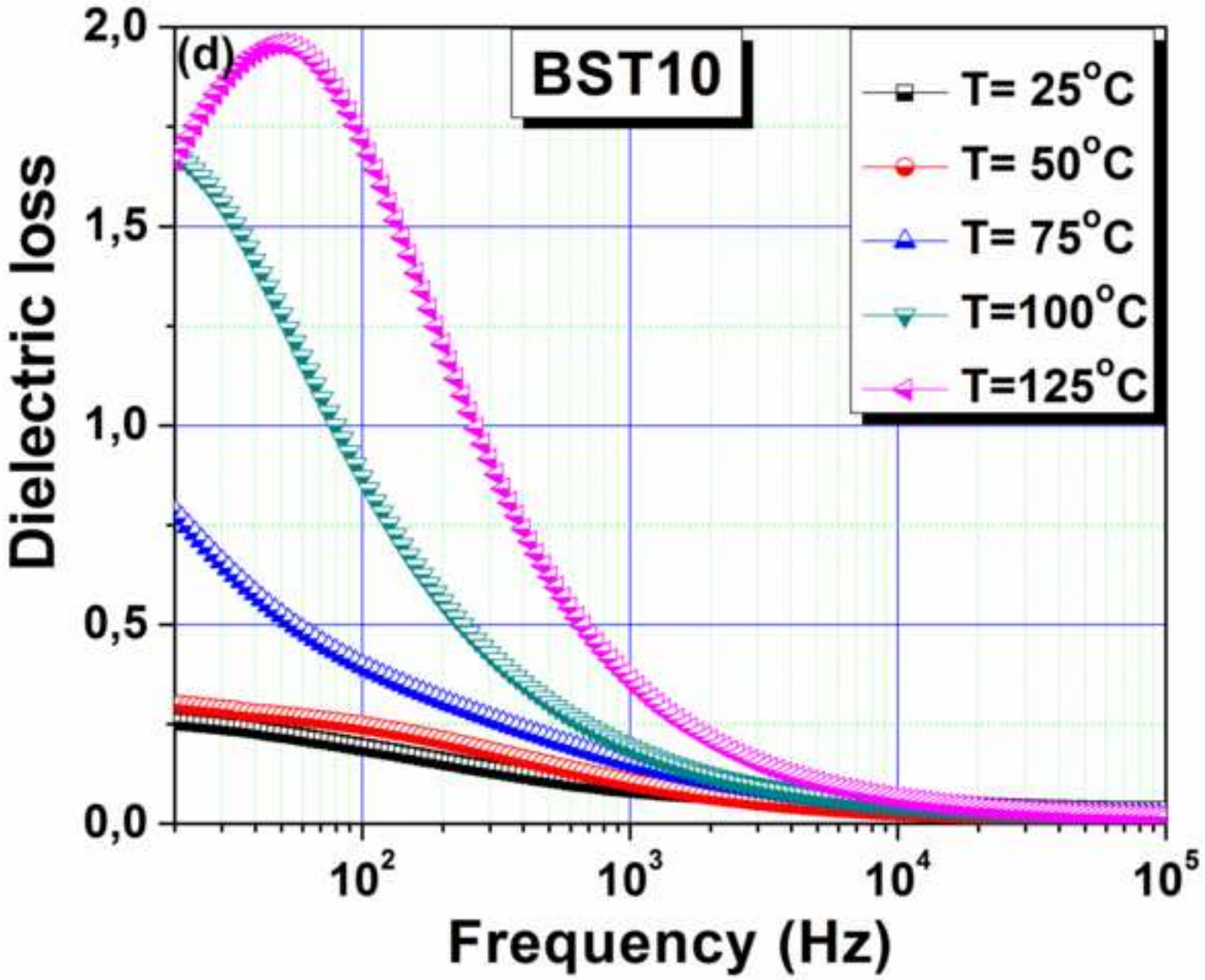
(d)
BST10
T= 25°C
T= 50°C
T= 75°C
T=100°C
T=125°C
Dielectric loss
2,0
1,5
1,0
0,5
0,0
10^2
10^3
10^4
10^5
Frequency (Hz)

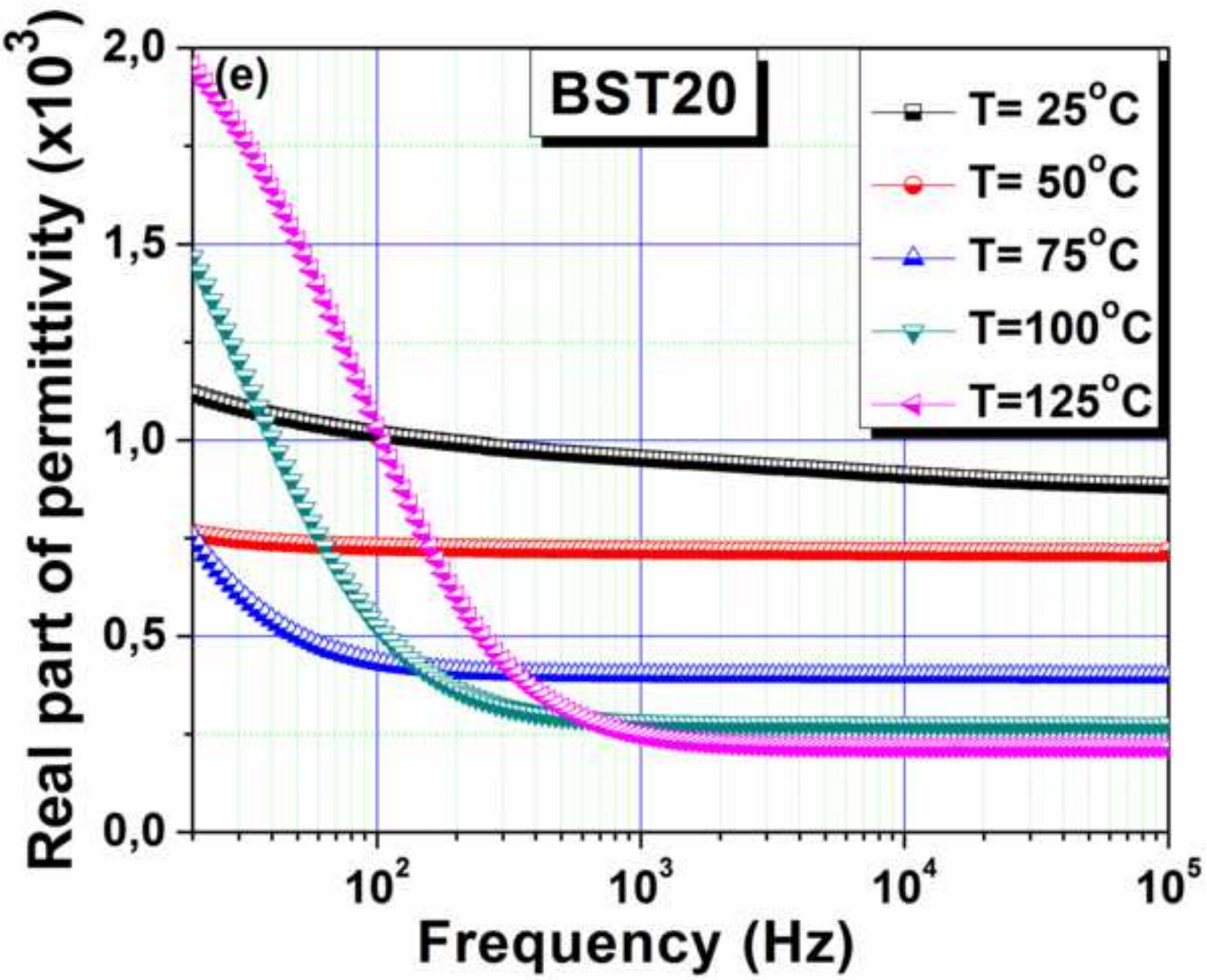
(e)
BST20
T= 25°C
T= 50°C
T= 75°C
T=100°C
T=125°C
Real part of permittivity (x10^3)
2,0
1,5
1,0
0,5
0,0
10^2
10^3
10^4
10^5
Frequency (Hz)

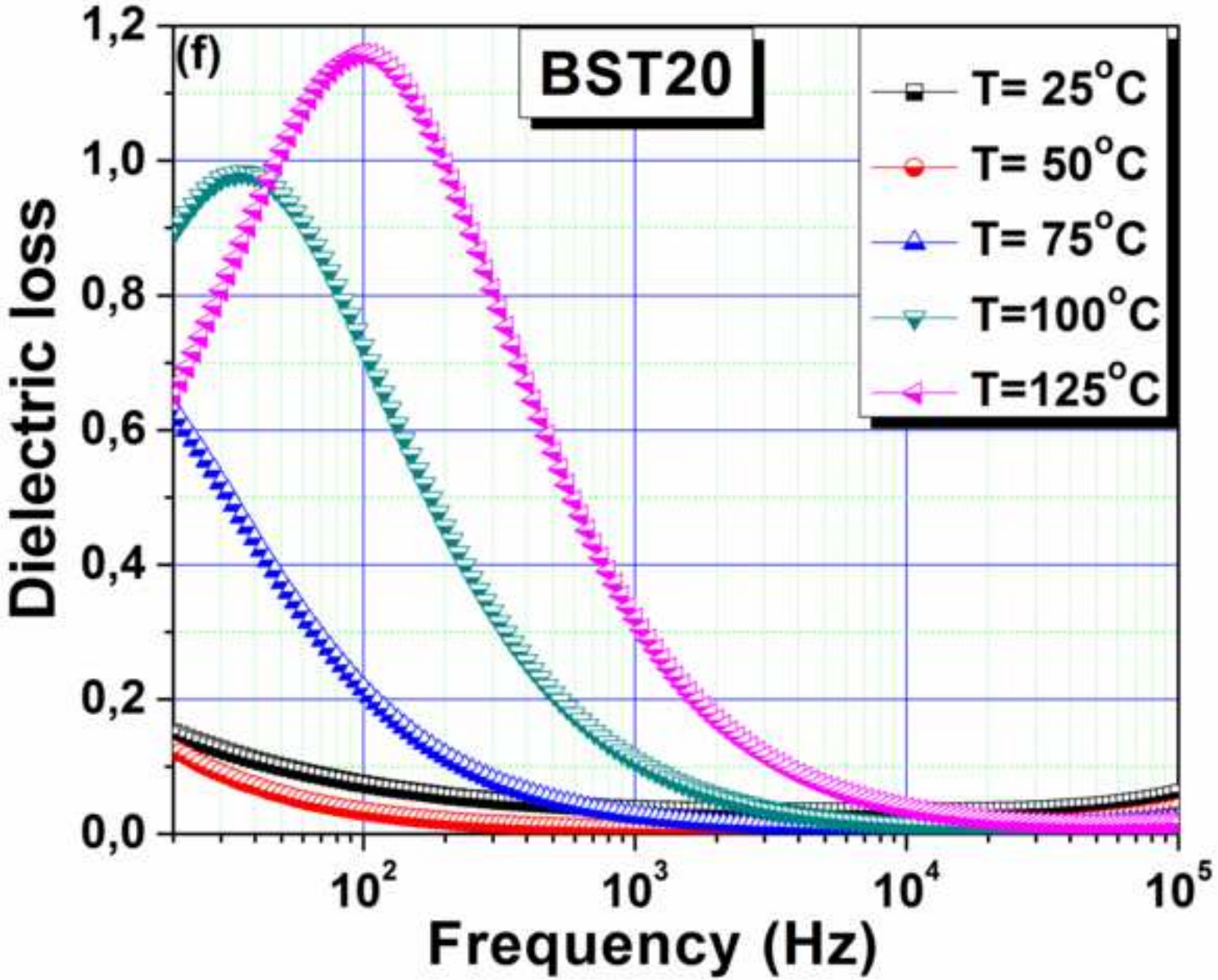
(f)
BST20
T= 25°C
T= 50°C
T= 75°C
T=100°C
T=125°C
Dielectric loss
1,2
1,0
0,8
0,6
0,4
0,2
0,0
10^2
10^3
10^4
10^5
Frequency (Hz)

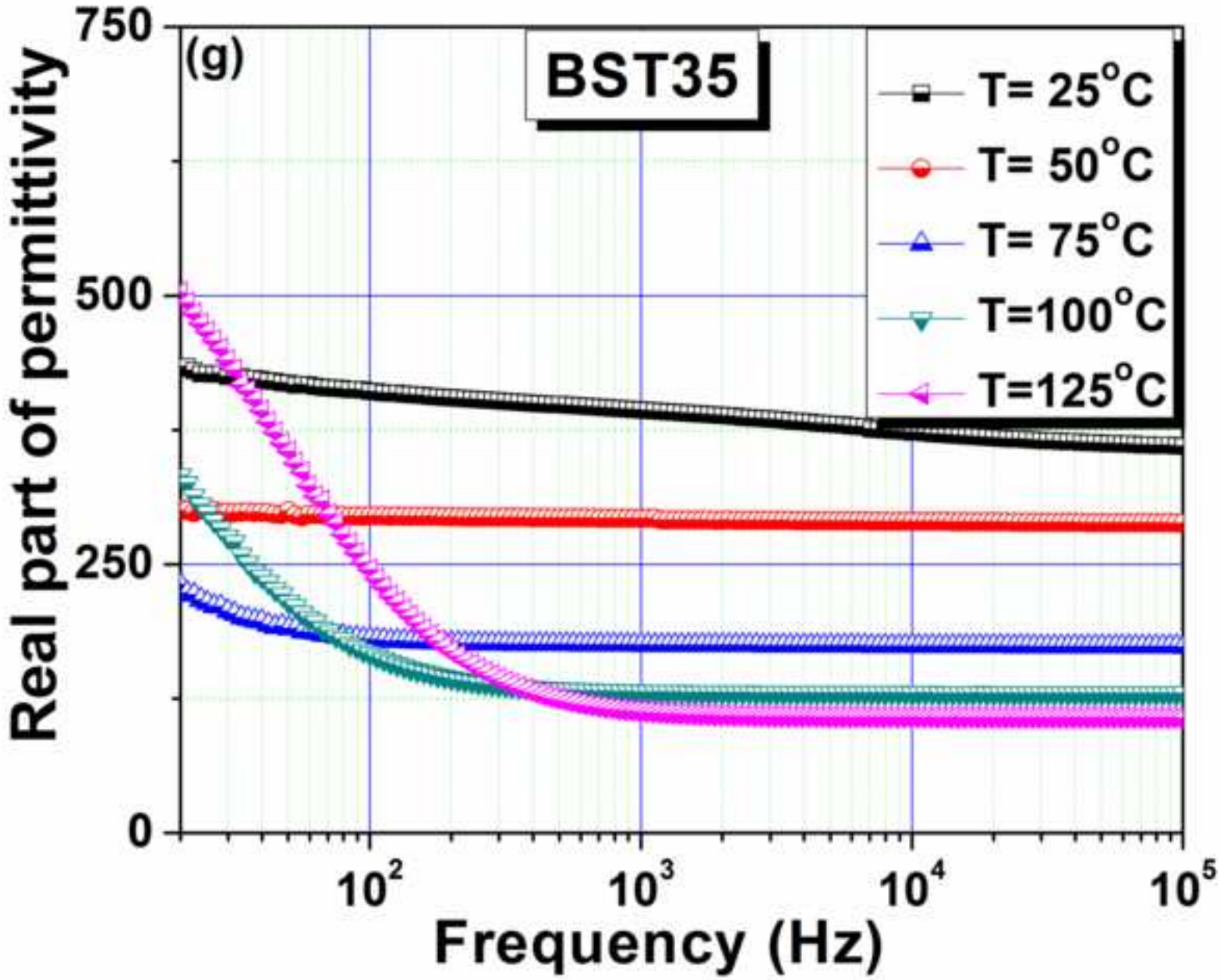

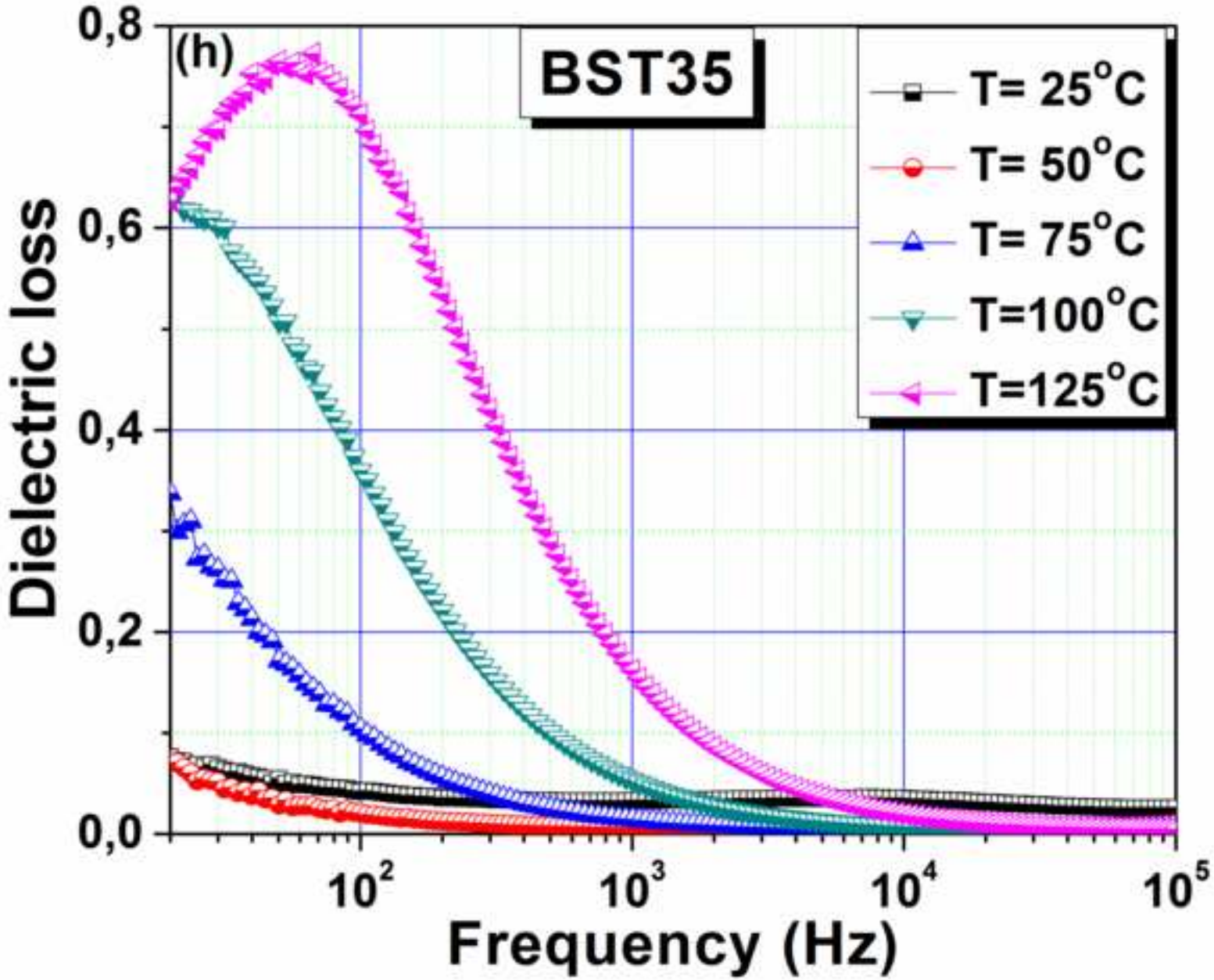

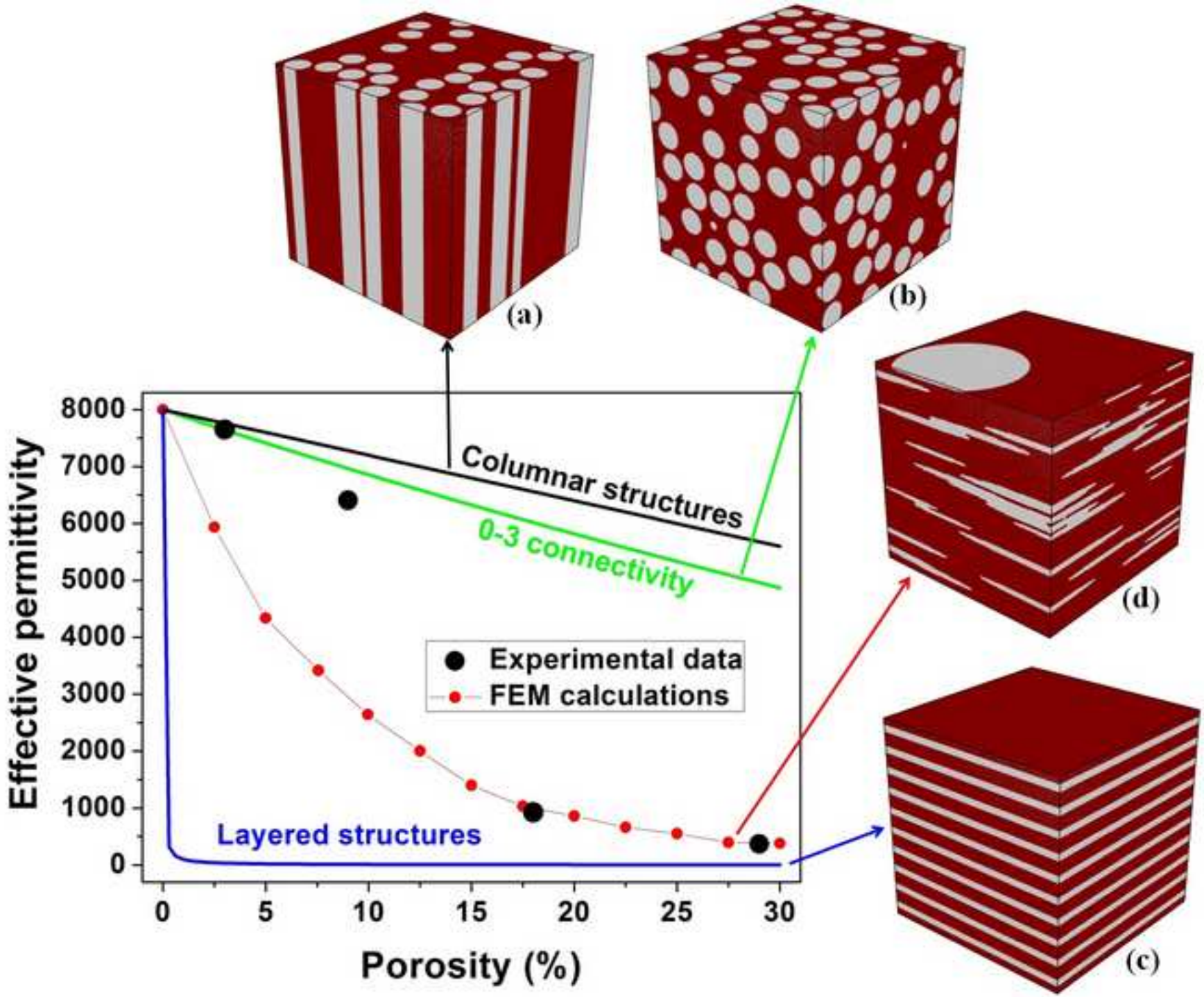

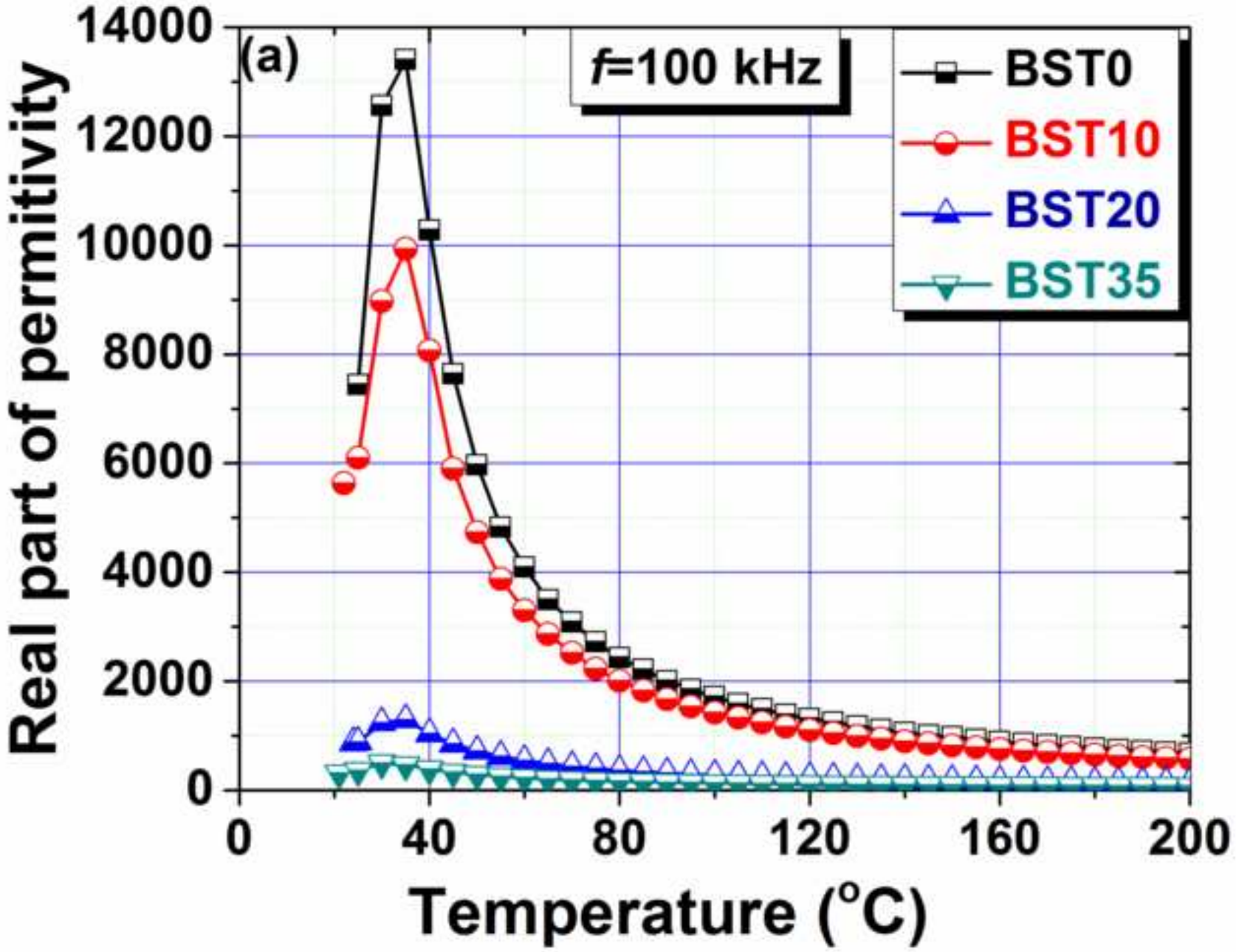

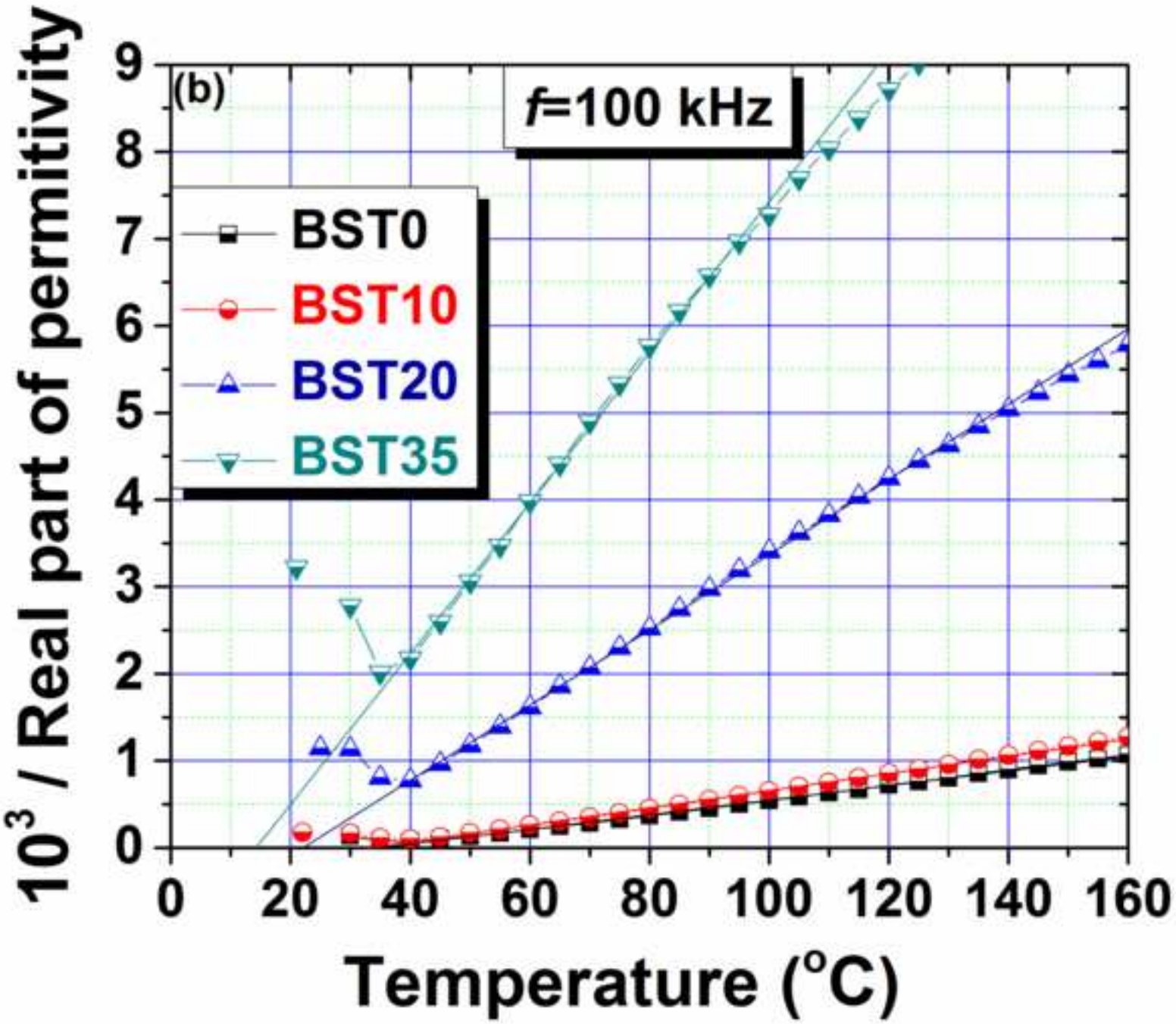

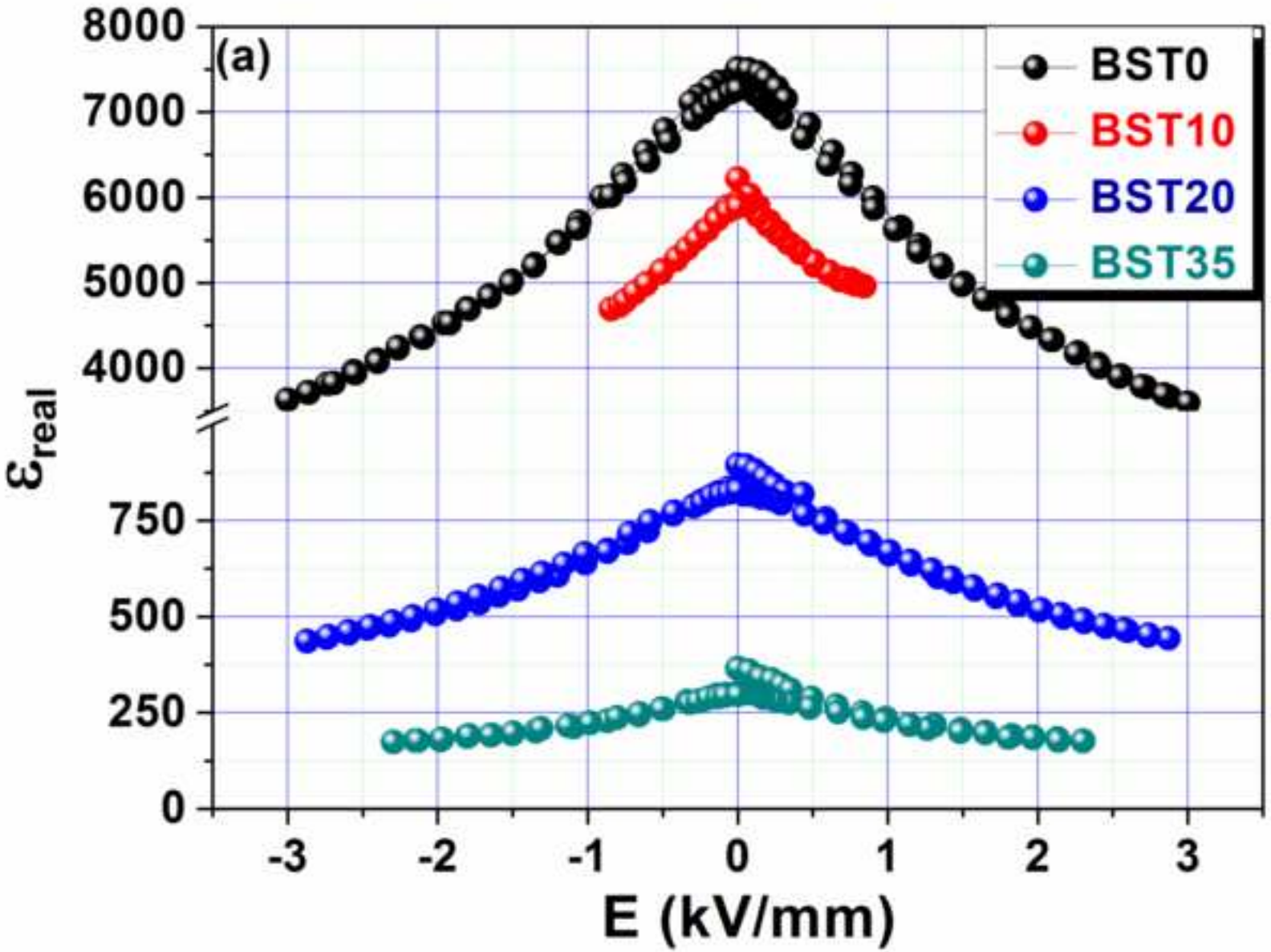
(a)
BST0
BST10
BST20
BST35
ε_{real}
8000
7000
6000
5000
4000
750
500
250
0
-3
-2
-1
0
1
2
3
E (kV/mm)

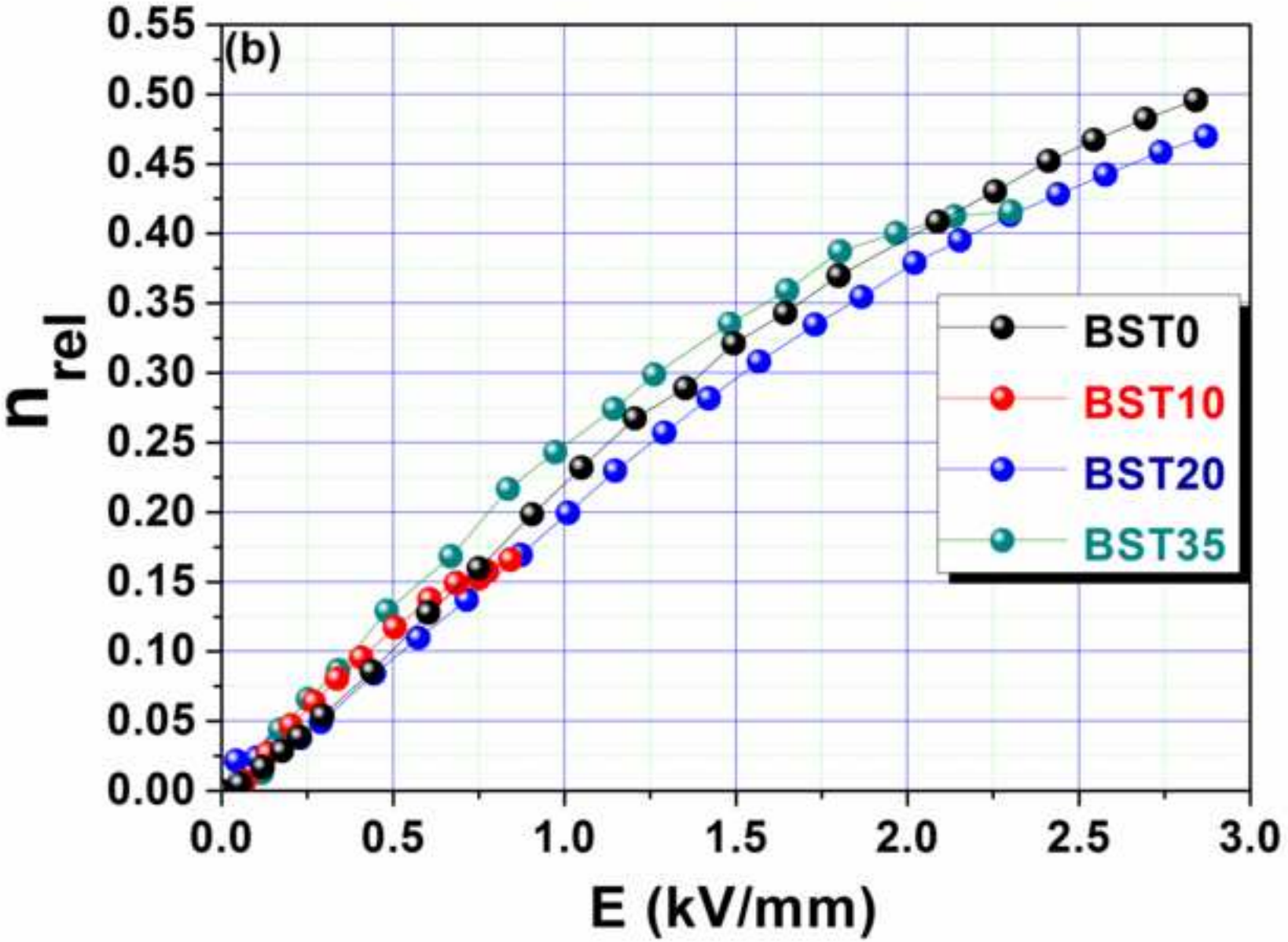

% graphite	Lattice parameter (Å)			c/a
	a	b	c	
0	4.0057	4.0057	4.0232	1.0043
10	4.0040	4.0040	4.0132	1.0023
20	3.9984	3.9984	4.0068	1.0021
35	3.9958	3.9958	4.0007	1.0012

Table 1. Lattice parameter of the BST investigated samples, from Rietveld refinement.

BST samples	Graphite addition (vol.%)	Sample porosity (vol.%)	Curie constant (1/slope)	T_0 (°C)	T_C (°C)
BST0	0%	3%	119094	35	35
BST10	10%	9%	101560	33	
BST20	20%	18%	23126	22	
BST35	35%	29%	11551	14	

Table 2. Computed Curie Weiss temperature and Curie constant for $Ba_{0.7}Sr_{0.3}TiO_3$ ceramics with different porosities.

Research Highlights

- Dense or porous $Ba_{0.70}Sr_{0.30}TiO_3$ ceramics were prepared by solid state reaction.
- Role of porosity on low and high field dielectric properties was investigated.
- The effective permittivity data was discussed in terms of EMA&FEM calculations.
- Permittivity is consequence of combined (0-3)–(0-3)&(2-2) phase interconnectivity.
- Relative dc-tunability is almost the same for dense and porous ceramics.